Experimental characterisation of the flow and turbulence generated by fractal oscillating grids

Valentin Musy,[1,2] Anne-Lise Hantson,[1] Diane Thomas,[1] Jean-Christophe Baudez,[2] and Tom Lacassagne[2]
[1)]*Chemical and Biochemical Process Engineering Unit, Faculty of Engineering, University of Mons, 7000 Mons, Belgium*
[2)]*IMT Nord Europe, Institut Mines Télécom, Univ. Lille, Center for Energy and Environment, F-59000 Lille, France*

(*Electronic mail: tom.lacassagne@imt-nord-europe.fr)

(*Electronic mail: valentin.musy@umons.ac.be or valentin.musy@imt-nord-europe.fr)

(Dated: September 20, 2024)

Inspired from the existing literature on fractal grids in channels and as an extension to classical oscillating grid experiments with simple Cartesian grids, an original investigation of fractal oscillating grid turbulence is here reported. The flows generated by a simple Cartesian grid, a fractal Cartesian grid, a fractal square grid and a fractal I-shaped grid are studied using Particle Image Velocimetry. Three oscillation frequencies (0.5, 1 and 1.5 Hz) and three stroke amplitudes (0.02, 0.035 and 0.05 m) are considered. The flows are broken down into mean (time averaged), oscillatory (phase dependent) and turbulent contributions using the triple Reynolds decomposition. The oscillation frequency is found to linearly impact the intensity of the mean and the oscillatory flows and the root mean square values of the turbulent fluctuations. In turn, an increase of the stroke amplitude tends to change the topology of the mean and the oscillatory flows. The turbulence intensity is increased by the fractal nature of the grids and is impacted by the mean flow topology, especially for the fractal I-shaped grid for which turbulence is transported away from the grid wake region. The study of the turbulence length scales and spectra reveals that the scales of turbulence mainly depend on the stroke amplitude and the grid geometry. We thus show how fractal oscillating grids can be used to generate turbulence with tailored properties for fundamental studies and practical applications.

I. INTRODUCTION

Turbulence is ubiquitous in nature and industrial applications. Understanding turbulence beyond the isotropic and homogeneous framework proposed by Kolmogorov[27,28,45,57] remains, to this day, a challenge for scientists and engineers willing to design efficient devices and systems involving turbulent flows interacting with multi-physics phenomenon (heat and mass transfers, particle transport...). In particular, turbulence is known to be quite efficient in promoting mixing, which makes it a sought-after mechanism when designing stirring devices. Yet, optimizing the design of such compounds requires an accurate understanding of turbulence in non-homogeneous and/or non-isotropic conditions, its production mechanisms by the stirring object, its bulk properties, and the impact of the later on scalar transport. This comprehension finally leads to the capability of controlling the flow, the turbulence properties, and the mixing process.

Many classical configurations in the process industry involve turbulence generation by one or several rotating impellers[17,49]. This design generates turbulence together with a mean rotational flow, which promotes mixing at both large and small scales, but at the cost of a significant shear stress imposed at the impeller location and vicinity. The latter can be detrimental when the fluid to be mixed is itself shear-sensitive or mechanically degradable or if shear-sensitive particles - like living cells[42,62], biochemical molecules[14] or crystals[10,69] for example - are suspended and transported in the fluid.

From a more fundamental standpoint, a challenge has always been to disentangle the effects of mean flow, turbulence, and coherent structures on transport properties and mixing and to understand as a first instance turbulence alone in its simplest homogeneous and isotropic form. Fixed grids in wind tunnels or water channels, either classical[8,25], fractal[22,31], or active[24,40,64], offer the possibility of generating high Reynolds number turbulence with significant homogeneity and isotropy but associated with a strong mean flow and thus relatively low turbulent-to-mean kinetic energy ratios. Devices such as oscillating grids[19,56,65] or randomly actuated jets[6,59] allow to generate turbulence with low to negligible mean flows in initially quiescent fluids, though at lower Reynolds number and with underlying mean flows may still persist and remain hard to control[37]. The design of devices allowing fine control and tuning of flows with well known relative energy contents of mean flows, large scale coherent structures and turbulence thus remains to be achieved.

Based on previous studies demonstrating the interest of fractal geometries for fixed grid turbulence[22,31,63,64] and as an extension of classical oscillating grids, this work proposes the study of the new concept of fractal oscillating grids and the turbulent flows they generate with two main objectives. Firstly, establish how it can be used as a tool for the fundamental study of turbulence and its interactions with other phenomena. Secondly, pave the way towards the use of fractal oscillating grids as efficient mixing devices for bio-process applications. In what follows, the general principles of oscillating grid turbulence in its well known configuration with simple Cartesian grids are first recalled in section II. Section III then presents the experimental setup and measurement techniques used in this study to analyse turbulence properties generated by four different grids oscillating at various frequencies and amplitudes in water, through statistical analysis of velocity

fields obtained by Particle Image Velocimetry (PIV). The result section (section IV) presents the characterisation of the mean, oscillatory, and turbulent flows created by the oscillating grids; a specific focus is made on turbulence properties. Finally, a conclusion summarises the main findings and highlights the potential of such fractal oscillating grids for the two aforementioned goals, namely controlled turbulence generation for fundamental studies and mixing intensification.

II. INTRODUCTION TO OSCILLATING GRID SYSTEMS

A. General description of a classical oscillating grid system

Fixed grids, composed of bars with square cross-sections, were used to study the turbulence they generate in wind and water tunnels[66]. This kind of grids can find an application as flow filters in water or gas channel. The generated turbulence by the interaction of the wakes behind the grid bars is assumed to be isotropic, all the more so at high Reynolds numbers, but weakens as the distance to the grid increases[8,25,26]. Therefore, the use of these fixed grids is limited for engineering applications, like mixing for example. Another more fundamental drawback of fixed grid turbulence is that this last one is inseparable from a strong mean flow (time averaged) from which it is derived and the turbulent kinetic energy is proportional to the pressure drop induced by the grid[25]. Therefore, it appears impossible to study purely turbulent flow by using fixed grids or at least with a weak mean flow compared to the turbulence intensity.

An alternative to fixed turbulence generating grids are the oscillating grids. These devices generate turbulence with manageable properties which have been largely studied by experimental works since several decades[65].

An example of the simplest experimental set-up to study oscillating grid turbulence (OGT) is depicted in figure 1. The grid, here immersed in a straight prismatic tank containing water with its base defined by the length of its sides L_{tank} and l_{tank}, is composed by crossed bars of length L_{bar} (if $L_{\text{tank}} = l_{\text{tank}}$, L_{bar} is unique) with a cross-section defined by a characteristic dimension l_{bar} (the side length for a square cross-section). The grid bars shape a mesh of size L_{mesh} (distance between the center of two square neighbouring grid openings or the distance between the lengthwise axis of two neighbouring bars) and is linked to an engine (with a rotation speed ω_{engine}, expressed in rad/s) by a rod-crank or a crankshaft system. Thus, the grid is given an oscillating translation motion normal to its plane around an equilibrium position z_{eq}. This periodic motion, typically sinusoidal, induces large jet flows through the grid openings and wakes by the bars travel in the fluid. Upon grid sweeping, the generated jet flows and wakes interact and form turbulence propagating away from the grid and spatially decaying with distance from the grid. The characteristic of the so-generated turbulence can be easily controlled thanks to the grid oscillation parameters: the grid oscillation frequency ν, expressed in Hz and the stroke amplitude (peak to peak) A, expressed in m.

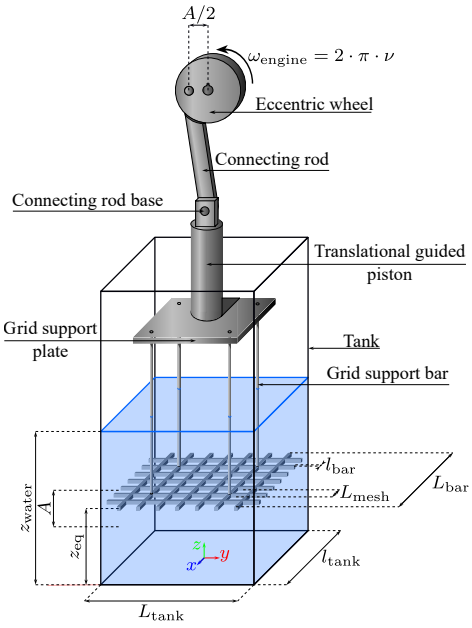

Figure 1. Simplest oscillating grid experimental set-up with one simple cross-barred grid (simple Cartesian grid) immersed in water.

B. Properties of the oscillating grid turbulence

The properties of the statistically steady oscillating grid turbulence are classically assessed through the prism of the flow statistics parameters such as the mean flow velocity $\overrightarrow{\bar{v}}$, the turbulent velocity fluctuations $\overrightarrow{v}$, the turbulent length and time scales, the Reynolds stress, the turbulent Reynolds numbers and the turbulent kinetic energy.

Thanks to hot film probe experiments, Thompson and Turner[56] were the first authors to propose a relation (equation 1) between the grid oscillation parameters (the stroke amplitude A and the oscillation frequency ν) and the intensity of the generated turbulence depicted by the root mean square (RMS) values of the statistically steady turbulent fluctuations of the horizontal velocity component $(v_x)_{\text{RMS}}$.

$$(v_x)_{\text{RMS}} = 1.4\ \nu\ A^{2.5}\ z_{\text{r}}{}^{-1.5} \tag{1}$$

This last relation expresses the turbulence intensity spatial decay away from the grid according to a relative vertical coordinate z_{r}; the reference point of this last one lies near the grid equilibrium position z_{eq} (the definition of this origin point is discussed later in this section). One may yet question the relevance of this relation as it does not involve geometric parameters of the grid. Thus, again thanks to hot film probes experiments, Hopfinger and Toly[19] proposed relations (equations 2 and 3) for the RMS values of the turbulent fluctuations of the

horizontal and vertical velocity components involving the grid mesh size L_{mesh}.

$$(v'_x)_{\text{RMS}} = (v'_y)_{\text{RMS}} = k_{xy}\, {L_{\text{mesh}}}^{0.5}\, \nu\, A^{1.5}\, {z_{\text{r}}}^{-1} \tag{2}$$

$$(v'_z)_{\text{RMS}} = \frac{k_z}{k_{xy}}\, (v'_x)_{\text{RMS}} = k_z\, {L_{\text{mesh}}}^{0.5}\, \nu\, A^{1.5}\, {z_{\text{r}}}^{-1} \tag{3}$$

Hopfinger and Toly[19] estimated the proportionality constants k_{xy} and k_z respectively equal to 0.25 and 0.27, while De Silva and Fernando[53,65] proposed $k_{xy} = 0.22$ and $k_z = 0.26$; in any case, this indicates the nearly isotropic turbulence generated by oscillating grid systems despite the slight prevalence of the vertical velocity component. The proportionality between the RMS values of the velocity fluctuations and ${z_{\text{r}}}^{-1}$ and the turbulence isotropy are largely accepted beyond about twice[4,68] or three times[7] the grid mesh size L_{mesh} away from the grid equilibrium position z_{eq}; another distance often mentioned is four times the strokes amplitude[44] A. The linear relation between the RMS values of the turbulent velocity fluctuations and the frequency[38,43] ν remains valid for frequencies below approximately 7 Hz.

About the turbulence length scales, Thompson and Turner[56] established a direct linear relation between the integral length scale L_I (associated to the size of the largest eddies in the statistically steady flow) and the relative coordinate z_{r} with a proportionality constant k_I estimated at 0.1 (see equation 4). This linear relation was later confirmed by Hopfinger and Toly[19] who show a direct linear relation between the proportionality constant k_I and the stroke amplitude A too.

$$L_I \propto k_I\, z_{\text{r}} \tag{4}$$

An estimation of the smallest turbulence time scale, the Kolmogorov time scale t_{K}, was computed thanks to the Hopfinger and Toly's results by Yi and Lyn[68]; it lies between 0.01 and 0.1 s.

While Thompson and Turner[56] defined the reference point of the z_{r} coordinates 0.01 m below the grid equilibrium position z_{eq}, Hopfinger and Toly[19] proposed a more general definition: the reference point matches with the zero of the straight line obtained by linear regression of the integral length scale data according to the absolute vertical coordinate z. By this procedure, the reference point lies close to the equilibrium position of the grid z_{eq}, so close that it is therefore commonly assumed that the reference point matches with the grid equilibrium position[68] z_{eq}.

By considering ρ as the fluid density (expressed in kg/m^3) and μ as the fluid dynamic viscosity (expressed in Pa s) and combining the Thompson and Turner's relation (equation 1) or the Hopfinger and Toly's relations (equations 2 and 3) with the equation 4, one may obtain expressions for the turbulent Reynolds number Re_I based on the RMS value of the turbulent fluctuations of velocity and the integral length scale of turbulence. The first combination (with the equation 1) leads to an expression (equation 5) indicating a decay law of Re_I with the distance to the grid equilibrium position while the expression (equation 6) obtained with the second combination (with the equations 2 and 3) indicates that Re_I is independent of z_{r}. This second case is more in line with Hopfinger and Toly's results[19].

$$\text{Re}_I = \frac{(v'_x)_{\text{RMS}}\, L_I\, \rho}{\mu} = 1.4\, \nu\, A^{2.5}\, {z_{\text{r}}}^{-0.5}\, k_I\, \rho\, \mu^{-1} \tag{5}$$

$$\text{Re}_I = k_{xy}\, {L_{\text{mesh}}}^{0.5}\, \nu\, A^{1.5}\, k_I\, \rho\, \mu^{-1} \tag{6}$$

Again, by replacing the Hopfinger and Toly's relations for the RMS values of the turbulent fluctuations of velocity in the definition of the turbulent kinetic energy[44], it is possible to obtain an expression (equation 7) for the spatial decay of this last one involving a -2 exponent for the relative coordinate z_{r}. This relation seems consistent with the Hopfinger and Toly's results[19], especially beyond a distance away from the grid equilibrium position equal to twice the grid mesh size or four times the stroke amplitude[44,65] A.

$$E'_k = \frac{1}{2}\, \left({(v'_x)_{\text{RMS}}}^2 + {(v'_y)_{\text{RMS}}}^2 + {(v'_z)_{\text{RMS}}}^2 \right)$$

$$\Leftrightarrow E'_k = \frac{1}{2}\, \left(2\, {k_{xy}}^2 + {k_z}^2 \right)\, \left(L_{\text{mesh}}\, \nu^2\, A^3\, {z_{\text{r}}}^{-2} \right) \tag{7}$$

Due to the low values of the Reynolds stress component $\rho\, \overline{v'_x\, v'_z}$, several authors[7,44] assume that oscillating grid flows can be considered shear-free away from the grid wake region. The Reynolds stresses are almost null 0.1 m away from z_{eq} and reached their highest value (0.25 Pa) 0.05 m away from z_{eq}.

In addition, oscillating grid flows are considered shear-free due to the weak mean (time averaged) flow $\overrightarrow{\overline{v}}$ generated compared to the turbulence intensity[35,65]. However, the mean flow is not strictly null and it can interact with the turbulent flow inducing bias in the spatial turbulence decay away from the grid wake region. Some oscillating grid set-up configurations are prone to generate a more intense mean flow: if the grid solidity[16,65] (also called the blockage ratio, the ratio between the area developed by the bars S_{bar} and the total area of the grid S_{tot}, it means the grid bar surface plus the openings surface) is higher than 0.4, if the grid bar ends are such that the tank walls do not shape a symmetry plane[7,16,19,37], if z_{eq} is larger[11] than L_{tank}, if ν is greater[68] than 7 or 8 Hz and if A is greatly larger[61,68] than L_{mesh}. The origin of the mean flow seems intrinsic to the oscillating grid experiments in water boxes and seems to be linked to the initial condition of a considered experiment[39] and to the limit conditions imposed by the tank walls[36,37].

Oscillating grids were and are still mostly used for experimental research purpose. The properties of the oscillating grid turbulence were studied to enhance the fundamental understanding about turbulence mechanisms and, in addition, these turbulence properties encountered applications in specific research topic. Among these applications (see the review by[65]), studies of interfacial mixing and stratified flows commonly found in the environment[5,18,19,38,43,48,53,56] and studies of sediments transport and particles sedimentation[9,34,44,58]

were the first investigations involving oscillating grids. More recent studies were focused on chemical and biochemical engineering subjects such as the interactions between bubbles and OGT[41,67], the microorganism cultures[1,3,50] or the impact of OGT on biofilms[33].

The most intuitive extensions to the simplest oscillating grid system (with one simple Cartesian grid) are systems composed by two simple grids oscillating in phase or in phase opposition[20,51,52] or multi-grid systems[32]. Such a system can come handy for emphasising the region of approximate turbulence homogeneity and isotropy lying between the two oscillating grids instead of studying the turbulence decay away for the grid. But without adding extra grids, another way to modify the nature of the grid generated flow is to change the geometry of the grid itself, in an approach similar to what has been done in the last decades for fixed grids in wind tunnels. Thus, the aim of this study is to investigate the flow and turbulence properties generated by an oscillating grid system composed with one grid with a fractal geometry. With a simple Cartesian grid as reference case, three fractal geometries, described in the following section, were investigated thanks to a Particle Image Velocimetry (PIV) method, also described in the following section, to visualise the generated flows. To the best of the authors' knowledge, the present work constitutes the first experimental implementation of fractal oscillating grid flows. The continuation of this article is structured as follows: the third part describes the experimental apparatus, the measurement techniques and the data analysis procedures while the fourth part summarises the main results obtained with four fractal oscillating grids (described in the third part).

III. EQUIPMENT AND FLOW VISUALISATION METHOD

A. General description of the experimental set-up and of the grid geometries

To achieve this study of the flow and turbulence generated by a fractal oscillating grids, an experimental set-up similar to the classical oscillating grid system depicted in the figure 1 was used. The used glass tank was 0.45 m high and had a square base with $L_{\text{tank}} = l_{\text{tank}} = 0.249$ m. For each experiment, it was filled with demineralised water in such a way that $z_{\text{water}} = L_{\text{tank}} = 0.249$ m; the water volume was therefore cubic. Regardless of the grid geometry, the oscillation frequency or the stroke amplitude, the grid equilibrium position was set at the centre of the water volume; implying that $z_{\text{eq}} = z_{\text{water}}/2 = 0.1245$ m. The grids were hung in the water by four support rods and a support plate linked to the driving system by a vertical and translational guided piston. The oscillation frequency was set thanks to a rotation speed-regulated engine AKM32-E from Kollmorgen and the stroke amplitude thanks to eccentric wheels with several eccentric holes. For each studied grid, three oscillation frequencies: 0.5, 1 and 1.5 Hz and three strokes amplitudes: 0.02, 0.035 and 0.05 m were applied to the oscillating grid system during this experimental study; thus resulting in 9 possible combinations per grid. The choices of these oscillation parameters were guided by technical reasons related to the design of our experimental set-up (not prone to endure high oscillation frequencies) and considerations about a final biochemical application (culture of shear-sensitive microorganisms).

Four grids were used: one classical cross barred grid called the simple Cartesian grid hereinafter, and three grids with fractal geometries. The design of the fractal grids were firstly proposed by Hurts and Vassilicos[22] who used these fractal geometries to generate fixed grid turbulence in wind tunnels. As the fractal grids are composed by bars with various width l_{bar}, the generated turbulence can contain directly near the grid a wide range of scales inducing higher homogeneity and better mixing properties than classical simple Cartesian grids[22,31,63,64]. These grid designs are built iteratively from a base pattern composed of N_{bar} bars with a length $L_{\text{bar};0}$ and a width $l_{\text{bar};0}$. The base pattern is repeated at each fractal iteration i in 4 occurrences around it with scaling factors for the bar length and width constant for all the iterations, respectively $\text{ratio}_{L_{\text{bar}}}$ and $\text{ratio}_{l_{\text{bar}}}$ leading to bars of length $L_{\text{bar};i}$ and width $l_{\text{bar};i}$ (see equations 8 and 9). Three fractal base patterns were used: a cross pattern, a square pattern and a "I" pattern.

$$L_{\text{bar};i} = \text{ratio}_{L_{\text{bar}}}{}^{i}\, L_{\text{bar};0} \tag{8}$$

$$l_{\text{bar};i} = \text{ratio}_{l_{\text{bar}}}{}^{i}\, l_{\text{bar};0} \tag{9}$$

For each used grid, some design remarks should be mentioned. The simple Cartesian grid (used as a reference case) can be seen as a special case of a fractal cross pattern grid (therefore called a fractal Cartesian grid) with the width ratio $\text{ratio}_{l_{\text{bar}}} = 1$. Another remark about the two Cartesian grids is that the length ratio $\text{ratio}_{L_{\text{bar}}}$ can not be strictly constant and decreases iteration after iteration, otherwise the bar ends would not be aligned. Nevertheless, as an approximation, this length ratio can be considered constant over the different fractal iterations to design the Cartesian grids. About the fractal I-shaped grid, it should be mentioned that it is longer than it is wide; it cannot be inscribed in a square (unless if the bar width is null, which is not practically realisable). In addition, although this pattern has a horizontal and a vertical axis of symmetry, it does not present one in a diagonal direction (unlike the other two base patterns).

As a preliminary design good practice proposed by Corrsin in 1963 for fixed simple cartesian grids and transposed to oscillating cases[16,65], the grid solidity (the blockage ratio) should be less than 0.4 to guarantee the stability of the jet flows and wakes generated by the grid oscillation; otherwise, the wakes can deflect their axes and secondary flows and inhomogeneous turbulence can be promoted[53]. In the present study, the grid solidity was kept constant among the grids, which were designed with a solidity of 0.3 as a surface constraint. The second major geometry constraint is the total side length of the grids bounded by the water tank side length (0.249 m) and a gap of more or less 0.0075 m (depending on the grid considered) between the grid ends and the tank walls which were taken into account. In practice, the four grids were manufactured in poly(methyl methacrylate) 0.005 m thick plates by laser cutting.

The notion of mesh size L_{mesh} is often used to characterise a grid. For a simple Cartesian grid, it is simply the distance between the center of two neighbouring grid openings or between the lengthwise axis of two neighbouring bars. For fractal grids, this notion is not so direct and therefore Hurst and Vassilicos proposed the notion of equivalent mesh size $L_{\text{mesh;eq}}$ (see equation 10) based on the surface developed by the bars S_{bar}, the total surface of the grid S_{tot} and the total grid perimeter $\mathscr{P}_{\text{grid}}$.

$$L_{\text{mesh;eq}} = \frac{4\,S_{\text{tot}}}{\mathscr{P}_{\text{grid}}}\sqrt{1-\frac{S_{\text{bar}}}{S_{\text{tot}}}} \tag{10}$$

The table I summarises the properties of the four grids used for this experimental study of fractal oscillating grid flows.

B. PIV experimental set up

The flow properties were investigated by using two dimensions and two velocity components Particle Image Velocimetry (PIV). The water velocity was determined in a vertical two-dimensional plane leading to two-dimensional vector fields of the fluid velocity involving the two vector components in the vertical plane[46].

The figure 2 in its left-hand part depicts the application of the PIV method to an oscillating grid system. The fluid medium was illuminated thanks to a vertical laser sheet, as thin as possible (about 0.001 m thick, in order to limit the "out of plane" effects), generated by a continuous laser Ray-Power from Dantec Dynamics with a wavelength of 532 nm. For all the investigated cases, the laser sheet cuts the fluid domain and the grids at their center; this centered laser vertical plane is illustrated on the grid drawings of the table I by a green line for each grid. The fluid velocity was captured thanks to light-scattering particles dispersed in the fluid medium, the motion of which was assimilated to fluid particles motion and recorded by a camera. The local velocity can be computed by comparing the position of a same group of particles on two successive PIV images separated by a time interval Δt (time-resolved PIV). Thus, our water tank was sown with 50 μm polyamide particles at a concentration such that approximately 10 particles appeared per interrogation window of 32 by 32 pixels on the recorded images. In the worst case, it means by considering the largest stroke amplitude and the highest grid oscillation frequency with the polyamide density[60] at 1140 kg/m^3, the particle Stokes number[46] St is about 0.0007 indicating that the polyamide particles can be considered as fluid particles (as St is much less than 1). The motion of the seeding particles was recorded by a CMOS (Complementary Metal-Oxide-semiconductor) LaVision Imager M-lite 5M camera fitted with a band-pass filter at 532 nm in front of the lens to avoid the impact of parasitic light. During the PIV experiments, the recorded PIV images were collected on a computer running the LaVision DaVis software. This last one was used to control the camera in terms of exposure time, acquisition frequency and recording time. Although PIV was performed in a single frame mode and used a continuous laser (leading to an unique acquisition frequency), a PTU X (Programmable Timing Unit, not depicted on the figure 2) synchroniser, normally used to synchronise a pulsed laser and a double frame camera, was required as an intermediary between the computer and the camera to run the DaVis software. In order to avoid parallax errors, the camera stand was placed more or less 1.5 m away from the experiment tank and its optical axis was vertically aligned with the grid equilibrium position.

The camera was placed in front of the water tank to see the whole plane defined by the laser sheet in the fluid medium and vertically aligned with the equilibrium position of the grid z_{eq} in order to reduce parallax effects. For each experiment, the resolution of the PIV images, displaying only the square fluid domain illuminated by the laser sheet, was about 750 by 750 pixels. The exposure time was set at 3 ms while the acquisition frequency ν_{acq} depended on the grid oscillation frequency and the stroke amplitude. Indeed, the higher the image resolution, the lower the maximum acquisition frequency allowed by the camera; the image resolution limits the acquisition frequency. Thus, the highest available acquisition frequency, $\nu_{\text{acq}} = 180$ Hz for an image resolution of 750 by 750 pixels, was applied to the cases with the highest grid oscillation frequency investigated $\nu = 1.5$ Hz. For the other cases with lower grid oscillation frequencies (1 or 0.5 Hz), the ratio between ν_{acq} and ν, in other words the number of frames per grid oscillation period, was kept constant at 120 frames per period of grid oscillation. However, it should be mentioned that for the lowest stroke amplitude $A = 0.02$ m, the acquisition frequencies were divided by two to increase the sensitivity in the regions far from the grid where velocities are typically lower leading to otherwise almost undetectable particle displacements on two successive images; for $A = 0.02$ m, there were therefore 60 frames per period of grid oscillation. The table II details the acquisition frequencies for the different cases of stroke amplitude A and grid oscillation frequency ν; this table is valid for the four grids investigated. The recording time and the total number of PIV images are discussed in the following paragraph about the flow statistics.

C. Post-processing of the PIV images

To analyse the PIV images and obtain two dimensions and two components vector fields of the instantaneous fluid velocity, the Matlab app PIVlab[55] together with Matlab custom scripts for pre and post-processing were used. A custom Matlab script allowed to detect and track the grid (assumed to follow a vertical sinusoidal motion) location and mask the grid and the support bars on each image before the computation of the velocity fields (as illustrated by the upper right part of the figure 2). Thus, a moving mask is applied on each PIV image to hide the grid and the grid support bars from the PIV algorithm computing the instantaneous vector fields.

A Fast Fourier Transfrom (FFT) based multipass algorithm was chosen to compute the correlation matrices. Three passes were applied with decreasing interrogation window sizes and a 50 % overlap: 64 by 64 pixels for the first pass, 32 by 32 pixels for the second one and 16 by 16 pixels for the third and

Table I. Geometric characterisation of the four fractal grids used (the little white holes in the complete grid drawings indicate the mounting points of the grid support bars). For the Cartesian grids, the values in brackets at the ratio$_{L_{\text{bar}}}$ line indicate the decrease of the bars length ratios between the 3 or 4 fractal iterations. The horizontal green lines on the complete grid drawings indicate the centered PIV laser plane positions relative to the grid.

	Simple Cartesian	Fractal Cartesian	Fractal square	Fractal I-shaped
Base pattern	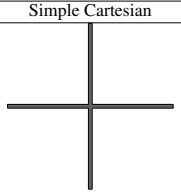	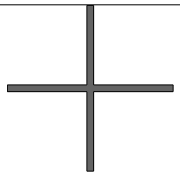	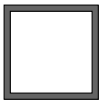	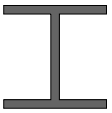
Complete grid	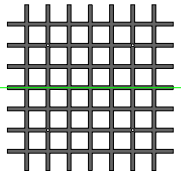	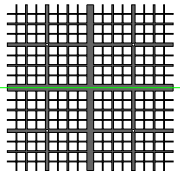	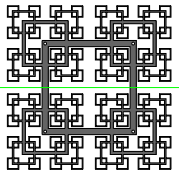	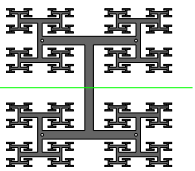
N_{bar}	2	2	4	3
$L_{\text{bar};0}$ [m]	0.2340	0.2340	0.1329	0.1451
$l_{\text{bar};0}$ [m]	0.0055	0.0095	0.0087	0.0121
ratio$_{L_{\text{bar}}}$	[0.488; 0.477]	[0.479; 0.478; 0.477]	0.500	0.426
ratio$_{l_{\text{bar}}}$	1.000	0.500	0.500	0.526
S_{bar} [m^2]	0.0164268	0.0164268	0.0164267	0.0155847
S_{tot} [m^2]	0.0547560	0.0547560	0.0547555	0.0519491
Solidity	0.3	0.3	0.3	0.3
$\mathscr{P}_{\text{grid}}$ [m]	6.9201	12.9502	14.8217	10.3156
$L_{\text{mesh;eq}}$ [m]	0.0299	0.0142	0.0124	0.0169

Table II. Acquisition frequencies ν_{acq}, expressed in Hz, applied for the different cases of strokes amplitude A and grid oscillation frequencies ν, valid for the four used grids.

	$A = 0.02$ m	$A = 0.035$ m	$A = 0.05$ m
$\nu = 0.5$ Hz	30	60	60
$\nu = 1$ Hz	60	120	120
$\nu = 1.5$ Hz	90	180	180

last one. The correlation peak of an interrogation window was estimated thanks to Gaussian sub-pixel estimator. A calibration, performed thanks to a scaling image and the knowledge of the time interval Δt between two successive PIV images (which is just the inverse of ν_{acq}), transforms the units of the vector fields from pixel/frame to m/s. At the end of the process, the instantaneous vector fields of fluid velocity have a resolution of more or less 90 by 90 vectors, leading to space discretisation steps Δx and Δz of more or less 0.0028 m.

Once all the instantaneous velocity fields computed, PIVlab post-processing functions were applied to remove the erroneous vectors. A first median filter threshold was applied on every instantaneous vector field to compare the two components of each vector with the components of its eight direct neighbours. A second standard deviation filter threshold checks if the two components of each vector lie in an interval of 3 times the standard deviation around the mean value of all the values of the considered velocity component for the considered frame. This way, only the erroneous and ludicrous vectors are removed according to the filter criterions; the valid vectors remain unchanged. Holes in the vector fields are subsequently filled by linear interpolation (between 3 and 7.5 % of the vectors are interpolated for each instantaneous flow field). Thus, only the masked regions (on the grid and the grid support bars) present no vector.

D. Flow statistics and Reynolds triple decomposition

The aim of the present work is to study statistically steady flow states generated by fractal oscillating grids. The implications are twofold: firstly, the oscillating grid system must be in operation for a sufficiently long time before the recording of the PIV images in stable conditions, to avoid any transient behaviour. At least 20 minutes after the start-up of the oscillating grid system were allowed before recording PIV images. Secondly, a sufficient number of PIV images are needed to

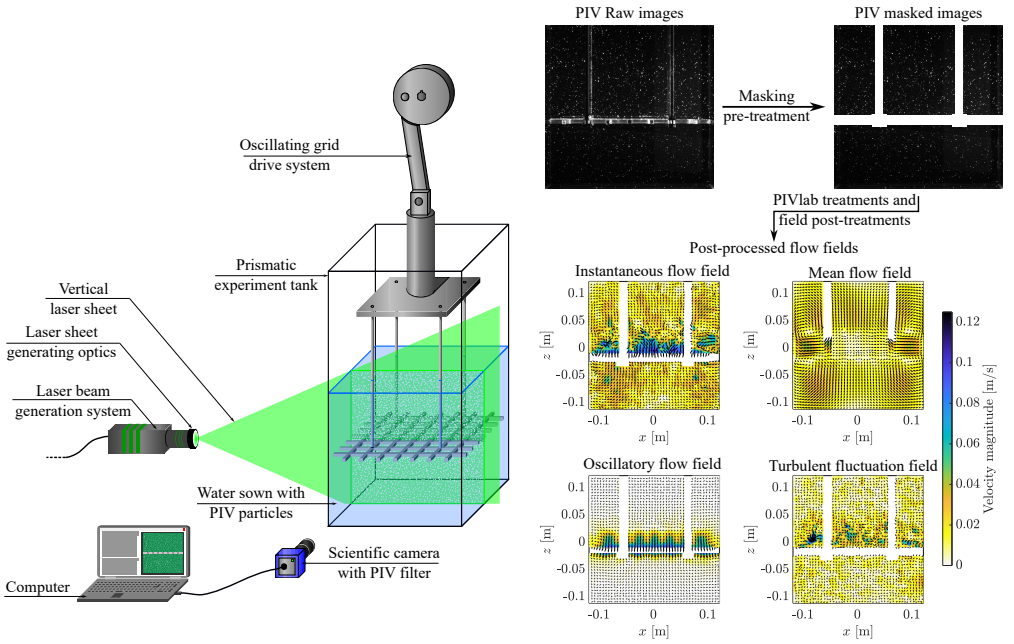

Figure 2. On the left, scheme of the two dimensions and two components PIV set up used to analyse oscillating grid flows. On the right, data processing: from the PIV raw images to the flow fields obtained by the triple Reynolds decomposition.

obtain converged velocity statistics. Thus, a preliminary convergence study for the flow statistics was performed and can be found in the appendix of this article. As the result of this convergence study, all the fractal oscillating grid experiments were performed by recording 1000 complete grid oscillation periods.

For all the experiments, fluid velocity data were analysed through the prism of the Reynolds triple decomposition, as originally proposed by Hussain and Reynolds[47] and subsequently applied to oscillatory flows[15,29]: the instantaneous flow field $\vec{\mathrm{v}}(x,y,z,t)$ is the sum of a time-independent mean flow $\overrightarrow{\overline{\mathrm{v}}}(x,y,z)$, an organised and phase-dependent oscillatory flow $\overrightarrow{\widetilde{\mathrm{v}}}(x,y,z,\varphi(t))$ and random turbulent fluctuations $\vec{\mathrm{v}}'(x,y,z,t)$ (see equation 11). This triple Reynolds decomposition of the flow fields is illustrated on the lower right part of the figure 2.

$$\vec{\mathrm{v}}(x,y,z,t) = \overrightarrow{\overline{\mathrm{v}}}(x,y,z) + \overrightarrow{\widetilde{\mathrm{v}}}(x,y,z,\varphi(t)) + \vec{\mathrm{v}}'(x,y,z,t) \quad (11)$$

In practice from two-dimensional and two components PIV images, the mean values of the flow are computed thanks by ensemble averaging, considering N_{fields} discrete instantaneous flow fields (see equation 12). The oscillatory flow is computed by the difference between the mean flow and the phase-averaged flow for each phase position $\varphi(t)$ computed thanks to 1000 discrete instantaneous flow fields (because each experiment is composed by 1000 grid oscillation periods) associated to the considered phase position (see equation 13). The instantaneous values of the turbulent fluctuations are easily deduced from the equation 11 and their RMS values are computed thanks to the equation 14.

$$\overline{\mathrm{v}_i}(x,z) = \frac{\sum_{t=0}^{N_{\text{fields}}} (\mathrm{v}_i(x,z,t))}{N_{\text{fields}}} \quad (12)$$

$$\widetilde{\mathrm{v}_i}(x,z,\varphi(t)) = \overline{\mathrm{v}_i}(x,z) - \overline{(\mathrm{v}_i)_\varphi}(x,z,\varphi(t)) \quad (13)$$

$$(\mathrm{v}_i')_{\text{RMS}}(x,z) = \sqrt{\frac{\sum_{t=0}^{N_{\text{fields}}} (\mathrm{v}_i'(x,z,t))^2}{N_{\text{fields}}}} \quad (14)$$

Several other classical turbulence features (turbulence spectra, length scales, ...) are discussed and detailed in the results part of this work in their respective associated sections.

IV. RESULTS

Let us recall that four grids were used for this experimental study of fractal oscillating grid flows: a simple Cartesian (considered as a reference case), a fractal Cartesian, a fractal

square and a fractal I-shaped grid (see table I). For each grid, the central vertical PIV plane was investigated and three grid oscillation frequencies ν (0.5, 1 and 1.5 Hz) and three stroke amplitudes A (0.02, 0.035 and 0.05 m) were applied to the oscillating grid system; it means 9 experiments per grid.

This results part is divided in sections dedicated to one flow property: the mean flow, the oscillatory flow, the turbulence intensity (RMS values of the velocity fluctuations), the turbulence length scales and the turbulence spectra. The impact of the grid oscillation ν and the stroke amplitude A are firstly discussed, directly followed by the impact of the grid geometry for each flow property.

The two-dimensional velocity field contours presented in the continuation of this article are depicted by colour gradients and show vertical white rectangles indicating that the associated points (x,z) were continuously covered by masks during the PIV treatments; therefore, no velocity values were associated to these points. The field values in the little regions directly underneath these white rectangles should be sparingly read as they were computed with a lower number of instantaneous values than the other points in the grid wake region. The velocity data depicted by these colour gradients were normalised by the maximum grid velocity $\max\left(v_{\text{grid}}\right) = A\,\pi\,\nu$ reached when the grid passes through its equilibrium position (by considering a vertical and sinusoidal movement for the grid). The vertical coordinates were normalised by the stroke amplitude A while the horizontal coordinates were normalised by the water tank side length L_{tank}. In addition, on these velocity field contours, the stroke amplitude is depicted by two horizontal outer black dotted lines whose vertical normalised coordinates z_r/A equal 0.5 and -0.5 (with z_r the relative vertical coordinates to the grid equilibrium position z_{eq}). The grid equilibrium position (at $z_r/A = 0$) is depicted too by a horizontal black dashed line and is surrounded by two other black horizontal lines indicating the thickness of the grid. For clarity reasons, only 1 vector out of 2 was drawn on the vector fields presented in this result section.

A. Study of the mean flows

For each oscillating grid experiment carried out, the mean flow was computed thanks to the equation 12 at each spatial point (x,z) of the vector fields.

The figure 3 presents the vector fields and the mean flow magnitude for the four grids and the three stroke amplitudes A with the grid oscillation frequency $\nu = 1$ Hz at the central vertical plane. Only the normalised mean flow fields for $\nu = 1$ Hz are reported in the results part of this article in order to avoid overloading results and since a change of the grid oscillation frequency ν appears to have a linear impact on the mean flow magnitude. Indeed, this linear impact of the grid oscillation frequency implies that the normalised (by the maximum grid velocity $\max\left(v_{\text{grid}}\right)$) mean flow is independent of ν in terms of magnitude and topology, at least in the frequency range investigated ($\nu = [0.5, 1, 1.5]$ Hz).

The impact of the stroke amplitude is much less trivial and non-linear. Indeed, the areas with a strong mean flow seem emphasised and magnified and some noticeable topological differences occur for each grid geometry for $A = 0.035$ and 0.05 m. These phenomena could be linked to the mesh size (or the equivalent mesh size) of the grids lower than these two large stroke amplitudes for the four grids (see table I). The difference between the impact of the stroke amplitude and the impact of the grid oscillation on the mean flows can be explained by the fact that a change in the stroke amplitude modify geometric properties of the experiment apparatus while it is not the case for the grid oscillation frequency.

Thus, for the simple Cartesian grid, the three central jets above and beneath the grid bars intersections, clearly recognisable for $A = 0.02$ m, tend to merge for larger stroke amplitudes. The jets generated by the most outlying bar intersections seem to be deflected and degenerate into large recirculation loops due to the nearby tank walls. The side recirculation zones induced by the bar edges in the grid wake region are growing in size and intensity with the stroke amplitude. Also in this grid wake region, the mean flow seems to converge toward the grid bar intersections, especially in the central zone where the recirculations induced by the bar edges become negligible. This convergence of the mean flow toward the centre of the water volume is only present horizontally in the grid wake region and vertically near the vertical tank walls; at any other point, the mean flow is directed away from the centre of the volume of water, toward the tank bottom or the water free surface. Thus, two kinds of mean flow structures could be distinguished: the ones apparently generated by the grid pattern itself (the three jets above the bar intersections in this case) and the ones resulting from the disturbance of the tank vertical walls (the large recirculations). The first ones are clearly recognisable only with a small stroke amplitude and seem to vanish or be submerged by the second ones. Those are magnified as the stroke amplitude increases and seem linked to the interaction between the bar edges and the tank walls.

The mean flows of the fractal Cartesian grid are similar to the simple Cartesian grid ones except that only one major jet above and beneath the central bar intersections (relative to the cross pattern at the first fractal level) seems noticeable and do not completely merge with other mean flow structures for large stroke amplitudes. The large recirculation loops due to the deflection of the jets near the tank walls and the side recirculations in the grid wake region generated by the biggest bar edges are clearly identifiable even with a small stroke amplitude; these phenomena seem to highlight the significance of the bar width. As for the simple Cartesian grid, the convergence behaviour in the grid wake region seems present too but only directed toward the largest bar intersections related to the first and the second fractal levels. Thus, the smaller bars and bar intersections (related to the third and fourth fractal level) seem to have a negligible impact on the mean flow. Thus, the significance of the mean flow structures seems clearly dependent on the grid bar width, especially for the mean flow structures related to the grid pattern, and the large recirculation loops are not only influenced by the tank walls.

The mean flows generated by the fractal square grid are unique compared to the mean flows produced by the three other grids: regardless of the stroke amplitude, the mean

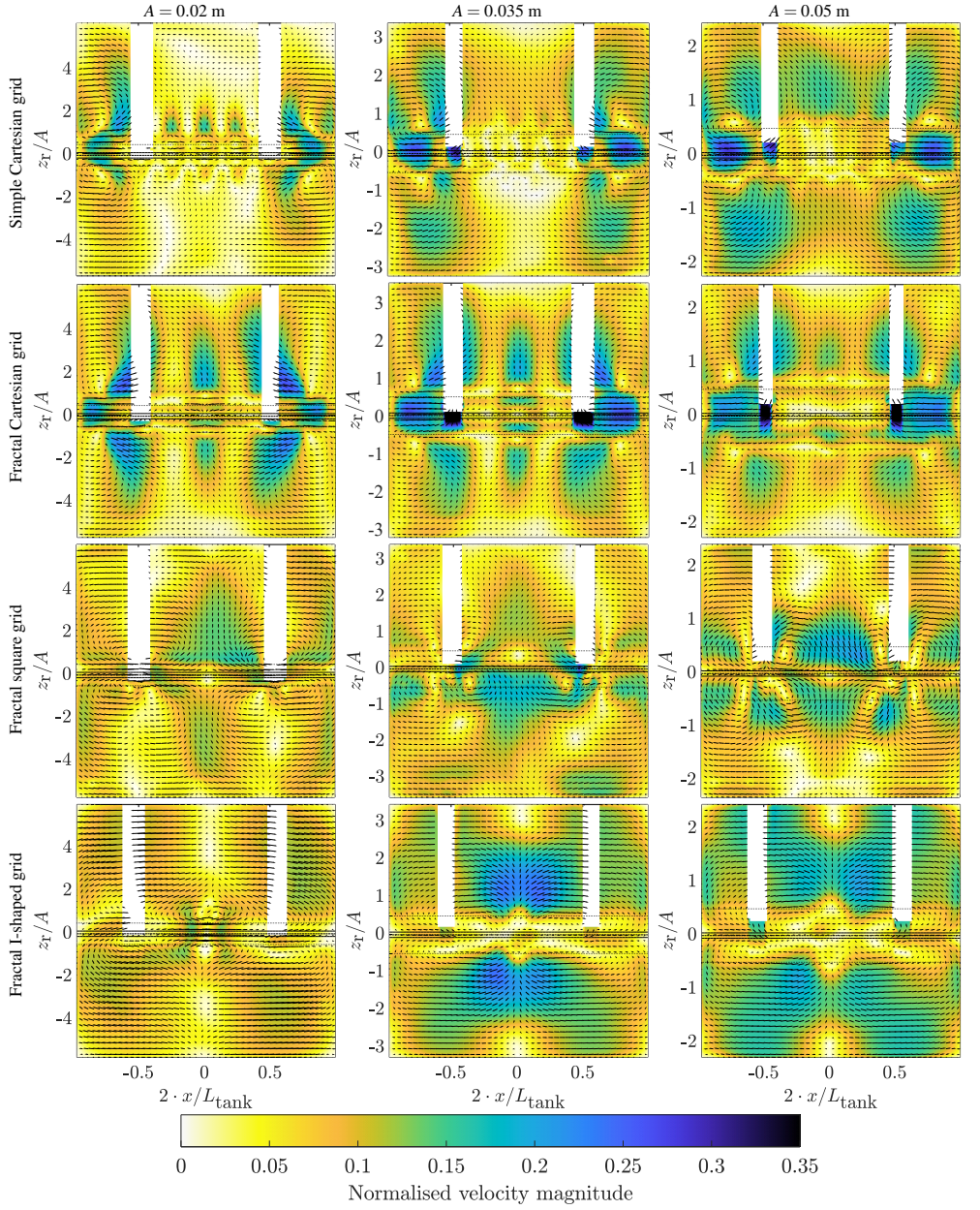

Figure 3. Vector fields and mean flow magnitude fields for the four grids and the three stroke amplitudes A with the grid oscillation frequency $\nu = 1$ Hz at the central vertical plane.

flow is always broadly directed toward the centre of the water volume; this indicates a quite pronounced three-dimensional mean flow structure and could be linked to the irregular hole distribution in the grid pattern (compared to the regular hole distribution of the Cartesian grids). Indeed, large central jets in the upper and the lower parts of the water tank are globally directed toward the grid equilibrium position to finally converge in the grid wake region between the two grid bars crossed by the PIV laser plane, like the side recirculation loops near the tank walls. The use of large stroke amplitudes ($A = 0.035$ and 0.05 m) seems to promote the emergence of large vortices at the limit of the grid wake region around the bars; the deployment of these vortices outside the square related to the first fractal level seems constrained by the tank walls. Conversely to the Cartesian grids, the flow structures mainly influenced by the tank walls do not seem to prevail over grid pattern related ones even when the amplitude increases. It could be explained by the irregular hole distribution of the grid pattern but also and especially by the fact that the grid bars near the tank walls are the thinnest ones (related to the last fractal iteration); this reinforces the hypothesis that the mean flow structures near the tank walls are due to an interaction between the grid edges and the tank walls.

The impact of the stroke amplitude on the mean flow is especially noticeable for the fractal I-shaped grid: with a small stroke amplitude ($A = 0.02$ m), the mean flow is converging toward the large central bar of the grid above and beneath this bar outside the grid wake region while it is directed toward the free surface and the tank bottom for larger stroke amplitudes ($A = 0.035$ and 0.05 m). For all the stroke amplitudes investigated, four large counter-rotating curls shape the general structure of the mean flow for this fractal I-shaped grid but their emergence seems depending on the stroke amplitude. Indeed, for larger strokes ($A = 0.035$ and 0.05 m), it seems that these curls are mainly induced by the diverging jets generated by the central bar of the grid while for a small stroke amplitude these curls appear to be more the result of a three-dimensional structure of the mean flow. This specific behaviour tends to confirm again our previous conclusions about the generation of the mean flow for the other grids. Indeed, as there is no grid bar near the tank walls for the fractal I-shaped in the central vertical PIV plane, the mean flow seems almost entirely influenced by the grid pattern and not by the interaction between the grid edges and the tank walls. Finally, we should mention that a drop in the mean flow magnitude seems to occur between $A = 0.035$ m and $A = 0.05$ m only for the fractal I-shaped grid. This drop can be explained by a more distant vortex shedding by the central grid bar magnifying the distant mean flow structures away from the grid wake region for $A = 0.05$ m or by an impact of the three-dimensional structure of the mean flow (already noticeable for the smallest stroke amplitude).

The dependence of the mean flow topology and intensity on the stroke amplitude, especially for the fractal I-shaped grid, can be linked to the Keulegan-Carpenter number KC classically used in the study of oscillatory flows[2,13,54]. This number involves a typical velocity of the oscillatory flow (the grid maximum velocity $\max\left(\mathrm{v}_{\mathrm{grid}}\right)$ in our case), the time period of the oscillatory flow (the inverse of the grid oscillation frequency ν) and a characteristic length: a bar width l_{bar}. Therefore, in our case, KC is independent of the grid oscillation frequency (see equation 15). For each grid, by considering the bar width of the first fractal iteration $l_{\mathrm{bar};0}$, one can obtain the values of KC reported in the table III. For the Cartesian grids and the fractal square grid, no change in the mean flow topology is reported in the relatively high investigated range of KC numbers. However, for the fractal I-shaped grid, the lowest KC number value ($KC = 5.2$) is related to an inversion of the global mean flow direction, suggesting a shift in the origin of the mean flow which depends only on the stroke amplitude and not on the grid oscillation frequency. The assumed critical KC number value for the simple Cartesian, fractal Cartesian and fractal square grids should be respectively below 11.4, 6.6 and 7.2 while this critical value for the fractal I-shaped grid lies between 5.2 and 9.1. This falls into the range of critical KC values reported in the literature in other flow contexts[2,13,54].

Table III. Values of the Keulegan-Carpenter number KC for each grid and stroke amplitude by considering the width of the first fractal iteration bars $l_{\mathrm{bar};0}$.

	$A = 0.02$ m	$A = 0.035$ m	$A = 0.05$ m
Simple Cartesian grid	11.4	20.0	28.6
Fractal Cartesian grid	6.6	11.6	16.5
Fractal square grid	7.2	12.6	18.1
Fractal I-shaped grid	5.2	9.1	13.0

$$KC = \frac{\max\left(\mathrm{v}_{\mathrm{grid}}\right)}{l_{\mathrm{bar}}\,\nu} = \frac{A\,\pi}{l_{\mathrm{bar}}} \tag{15}$$

B. Study of the oscillatory flows

The oscillatory flow was computed for each oscillating grid experiment at each available grid phase position $\varphi(t)$ (the total number of grid phase positions is defined by the ratio between the acquisition frequency and the grid oscillation frequency) and spatial point (x, z) of the vector fields by the difference between the mean flow and the phase-averaged flow (see equation 13).

The figure 4 presents the vector fields and the normalised velocity magnitude of the oscillatory flows for two odd phase positions - the lowest grid position and the equilibrium position when the grid is moving downwards - for $A = 0.02$ and 0.05 m with $\nu = 1$ Hz at the central vertical PIV plane. In our view, these two grid phase positions are sufficient to analyse the oscillatory flow as it is simply directed in the opposite direction by considering respectively the maximum grid position and the mean position when the grid is moving upwards. As for the mean flow, the impact of the grid oscillation frequency on the oscillatory flow topology and normalised magnitude seems not noticeable in the studied frequency range;

therefore only the cases with $\nu = 1$ Hz are considered on the figure 4. As for the mean flow, the influence of the stroke amplitude is more clear: the organised flow structures are larger and more intensive for large stroke amplitudes. However, these flow structures remain globally confined in the grid wake region outside which the oscillatory flows can be considered almost null. In all cases, the oscillatory flow is more intense behind the grid, especially for the grid extreme positions. As we could expect, the oscillatory flow magnitude is especially important when the grid passes through its equilibrium position and reaches its maximum velocity.

As the PIV central laser plane laterally cuts the grid bars for the fractal square and I-shaped grids, the oscillatory flow primarily consists of counter-rotating vortices around and behind the grid bars. These vortices, which have a horizontal size comparable to the width of the first fractal iteration bars, induce general rotary movements around the grid bars in the grid wake region. Therefore, the oscillatory flow is globally directed in the opposite direction to the grid movement. A completely different flow pattern is observed for the Cartesian grids as the PIV laser plane for the plane 0 cut the central grid bar in a lengthwise way. Thus, in this configuration, the oscillatory flow appears directed in the same direction as the grid movement and the flow patterns highlight the wakes induced by the meet of the counter-rotating vortices around and behind the grid central bars. These wakes are especially intense behind the grid bar intersections and seem to be deflected by the vortices around the grid bar edges. For the fractal Cartesian grid, the influence of the central grid bar seems too important and the vector field resolutions are not sufficient to clearly distinguish the impact of the intersection between the central bar and the finer bars.

C. Study of the RMS values of the flow turbulent fluctuations

The flow turbulent fluctuations $\vec{v}'$ stand for the remaining part of the flow after removing the mean flow $\overline{\vec{v}}$ and the oscillatory flow $\tilde{\vec{v}}$ (for the considered grid phase position $\varphi(t)$) from the considered instantaneous flow field $\vec{v}$ (see equation 11). As the turbulent fluctuations of the flow depict no clear flow pattern on instantaneous fields, it is analysed by considering its RMS values computed thanks to the equation 14.

The figure 5 presents the normalised fields of the RMS values of the turbulent fluctuations (horizontal and vertical components) for $A = 0.02$ and 0.05 m with $\nu = 1$ Hz at the central vertical PIV plane. Again and as for the mean and oscillatory flows, the grid oscillation frequency ν has no significant impact on the topology and normalised RMS values of the turbulent fluctuations in the considered frequency range and this is why only one grid oscillation frequency is considered on the figure 5. For the Cartesian grids, the impact of the stroke amplitude A is more noticeable in the grid wake region for the magnitude of the RMS values while the topologies remain similar for small and large stroke amplitudes. An increase of the stroke amplitude is more noticeable for the fractal square and I-shaped grids: the turbulent fluctuations are more intense near the grid bars and remain weaker away from the grid wake region for a small stroke amplitude while they seem to be transported away from the grid with larger stroke amplitudes. This behaviour seems to be linked to the mean flow. Indeed, for the fractal I-shaped grid, the increasing magnitude and the change in direction of the mean flow between small and large stroke amplitudes are fairly well superimposed on the propagation of the turbulent fluctuations away from the grid. Similarly for the fractal square grid, the propagation of the turbulent fluctuations away from the grid and their intense value in the grid wake region between the grid bars follow fairly well the large central jets and vortices around the grid bars at the limit of the grid wake region. This transport of the turbulent fluctuations by the mean flow seems present for the Cartesian grids but to a lesser extent.

The data presented on the figure 5 can be summarised by averaging the RMS values of the turbulent fluctuations line by line to obtain the vertical profiles $(v'_i)_{\mathrm{RMS}}(z)$ for which Hopfinger and Toly proposed equations (see equations 2 and 3). Thus, the figure 6 depicts these vertical profiles of the RMS values of the turbulent fluctuations $(v'_x)_{\mathrm{RMS}}$ and $(v'_z)_{\mathrm{RMS}}$ for the three used stroke amplitudes with $\nu = 1$ Hz at the central vertical PIV plane. The RMS values of the turbulent fluctuations were not normalised by the grid maximum velocity and only the cases with $\nu = 1$ Hz were considered on this figure for clarity reasons (to avoid excessive superimposition of curves). The Cartesian grids have similar behaviours: the turbulence intensity reaches its maximum near the grid equilibrium position and quickly fades away from the grid to a lesser degree for the fractal Cartesian grid. The turbulence intensity is always lower for the fractal square and I-shaped grids in the grid wake region and surroundings than for the Cartesian grids but the turbulence decay appears less steep, especially for the fractal I-shaped; at stated in the previous paragraph, this can be linked to a turbulence transport phenomenon by the mean flow. Thus, in a general way, one can say that the fractal nature of an oscillating grid tends to preserve the turbulence intensity far from the grid.

The graph on the right of the figure 6 and above the legend depicts the evolution of the isotropy coefficient, i.e the ratio $(v'_x)_{\mathrm{RMS}} / (v'_z)_{\mathrm{RMS}}$, along the vertical z_{r} coordinate. Whatever the grid geometry and amplitude, the values of this indicator lie between 0.75 and 1, which is consistent with the ratio between the Hopfinger and Toly's constants k_z and k_{xy}, especially for the values given by De Silva and Fernando[53] respectively 0.26 and 0.22. The predominance of the vertical turbulent velocity component tends to increase with the distance from the equilibrium position of the grid until the influence of the boundary conditions becomes significant at more or less 0.025 m before the tank bottom or the free surface. Although the grid geometry and the stroke amplitude seem to have no noticeable impact on the vertical profile of the isotropy coefficient, we should mention that the turbulence transport by the mean flow enhances the vertical component of the turbulent fluctuations for the fractal I-shaped grid with large stroke amplitudes just before the influence of the boundary conditions becomes significant. Other odd cases are the fractal square grid, especially with $A = 0.02$ m, in the grid

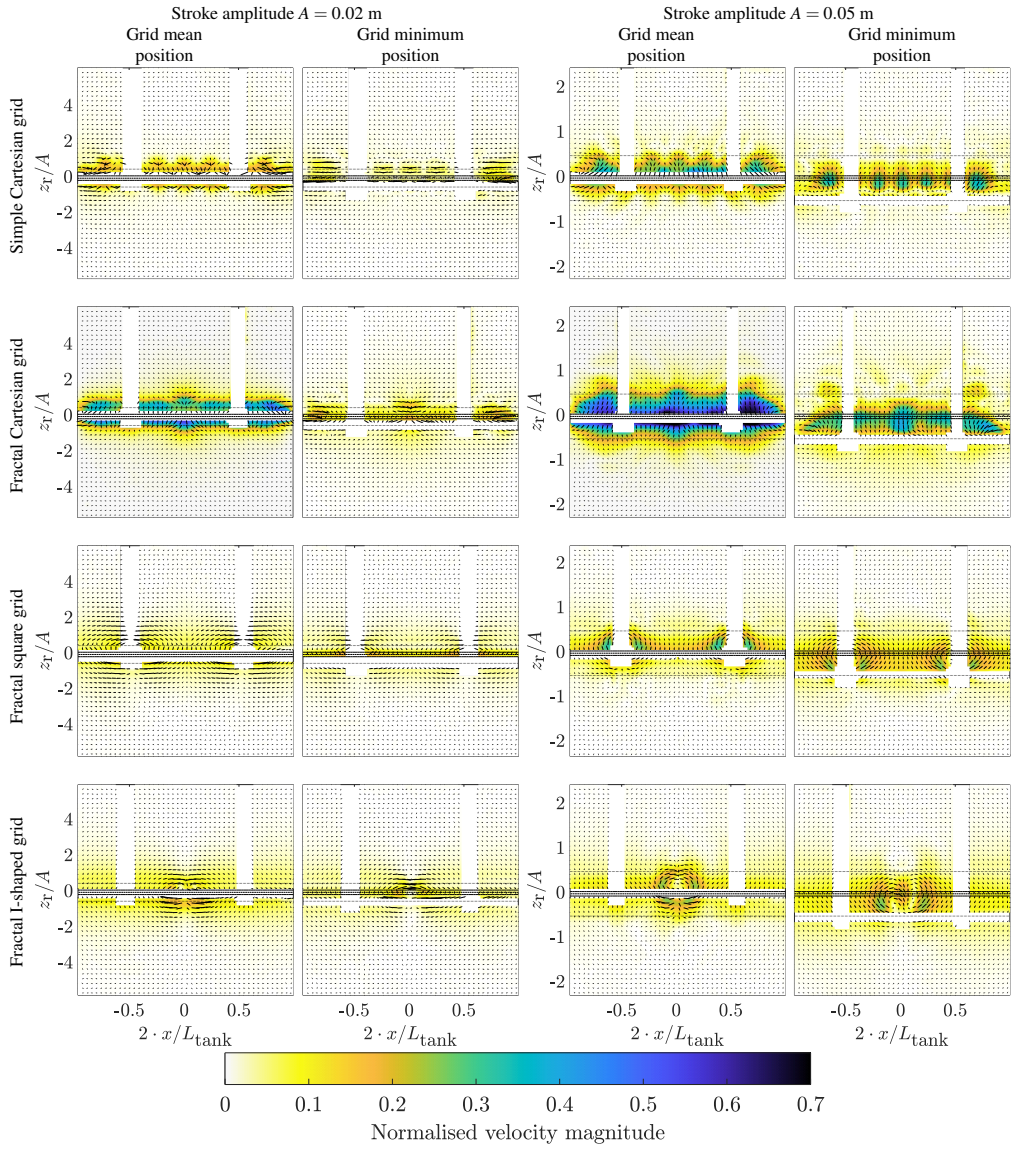

Figure 4. Vector fields and oscillatory flow magnitude fields for the four grids, for the smallest and the largest stroke amplitude investigated and for two singular grid positions (the grid mean position while it is going down and the grid minimum position) with the grid oscillation frequency $\nu = 1$ Hz at the central vertical plane. The horizontal white rectangles are due to the mask used during the PIV post processing.

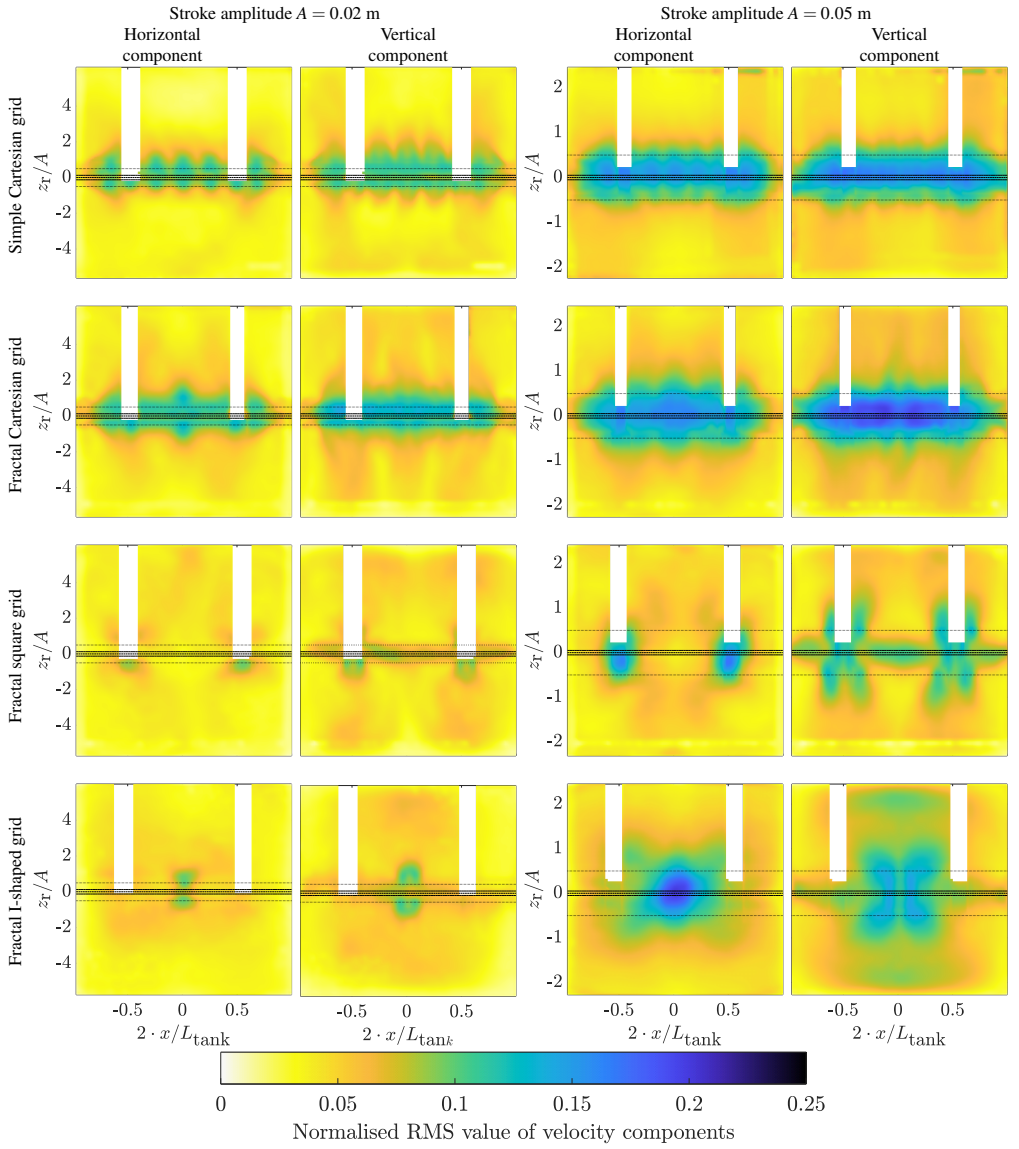

Figure 5. Normalised fields of the RMS values of the horizontal and vertical components of the turbulent fluctuations for the smallest and the largest stroke amplitudes A with the grid oscillation frequency $\nu = 1$ Hz at the central vertical plane.

wake region where the vertical component of the turbulent fluctuations seems promoted due to the mean flow direction.

The four graphs on the lower part of the figure 6 stand for the vertical profiles of the RMS values of the turbulent fluctuations $(v'_x)_{\mathrm{RMS}}$ and $(v'_z)_{\mathrm{RMS}}$ with the axis in logarithmic scales above and under the grid equilibrium position. Unlike their equivalents with the axis in linear scales, these graphs provide the possibility to clearly identify the decay rate of the turbulence intensity with the vertical distance to the grid equilibrium position and to verify the exponent of the z_r coordinates in the Thompson and Turner's equation or the Hopfinger and Toly's equations. For this purpose and in addition to the vertical profiles $(v'_i)_{\mathrm{RMS}}(z)$, straight lines are depicted with specific slopes of -0.8, the lowest value of the z_r exponent reported by Nokes[43,65], of -1, the classical value of the z_r exponent in the Hopfinger and Toly's equations (see equations 2 and 3) and of -1.5, the z_r exponent value proposed by the Thompson and Turner's equation (see equation 1). The curves related to the simple Cartesian grid present a better agreement with the -0.8 exponent, especially above the grid equilibrium position while the -1 exponent seems less accurate or at least on a smaller range of z_r values. The -1.5 exponent seems completely inaccurate in every cases. The impact of the boundary conditions seems important on these spatial decay law, especially the solid wall of the tank bottom which affects the turbulence decay for the horizontal and the vertical velocity components while the water free surface mainly impacts the vertical component. For the three other fractal grids, the models proposed by Hopfinger and Toly or Thompson and Turner for the spatial turbulence decay appear inaccurate as the exponents of z_r should be higher than -0.8. The disagreement between the experimental vertical profiles of the RMS values of the turbulent fluctuations and the empirical Hopfinger and Toly's equations can be explain by the presence of strong mean flows, especially for the three fractal grids and to a lesser degree for the simple Cartesian grid.

Although only three frequencies and three stroke amplitudes were analysed for the four grids, we propose to verify the exponents of ν and A in the Hopfinger and Toly's law. To achieve this, the RMS values of the turbulent fluctuations $(v'_x)_{\mathrm{RMS}}$ and $(v'_z)_{\mathrm{RMS}}$ were normalised by the parameters of the Hopfinger and Toly's equations in order to respectively isolate ν or A. Thus, the relation between $(v'_i)_{\mathrm{RMS}}\ z_\mathrm{r}\ A^{-1.5}\ L_{\mathrm{mesh}}^{-0.5}$ and ν should be linear with a slope equivalent to the Hopfinger and Toly's constants and a null intercept (set to 0 for the computation of the linear regression) while the slope and the intercept of the linear regression between $\log\left((v'_i)_{\mathrm{RMS}}\ z_\mathrm{r}\ \nu^{-1}\ L_{\mathrm{mesh}}^{-0.5}\right)$ and $\log(A)$ respectively stand for the A exponent and the logarithm of the Hopfinger and Toly's constants (set to -0.6576 for the horizontal component and to -0.5850 for the vertical component during the regression process). All the points presented on the figure 7 were obtained by averaging the vertical profiles of the RMS values of the turbulent fluctuations along the z_r axis. The slopes and the coefficients of determination R^2 obtained from the linear regressions displayed on the figure 7 are summarised in the tables IV and V.

About the frequency dependence, as the coefficients of determination are close to 1, the linear regressions fit quite well the experimental points for the four grids and the three stroke amplitudes used. For the simple Cartesian grid only, the three regression lines overlap indicating that the exponents of the other parameters (A, especially) are accurate too and the values of the slopes are in a good agreement with the values of the Hopfinger and Toly's constants proposed by De Silva and Fernando[53,65]. This linear dependence with the oscillation frequency ν can explain why it has a low impact on the normalised velocity values; this remark could be extended to the mean and oscillatory flows as ν seems to have no significant impact on the topology of the normalised velocity fields in the assessed range of oscillation frequencies. Since the regression lines do not overlap for the three other fractal grids, especially for the fractal I-shaped grid, the Hopfinger and Toly's laws seem to be unenforceable for these grids even though the linear impact of the frequency seems correct.

As said in the previous paragraph, the 1.5 exponent of A in the Hopfinger and Toly's laws seems correct for the simple Cartesian grid while a value lying between 1.36 and 1.39 seems accurate for the fractal Cartesian grid. For these two Cartesian grids, the three regression lines overlap confirming again the linear dependence with the oscillation frequency and partially validating the Hopfinger and Toly's laws. The same phenomenon appears for the fractal square grid with 1.4 for the A exponent. However for the fractal I-shaped grid, the linear regressions seem clearly less accurate than for the Cartesian grids and the fractal square grid (in view to the values of the coefficients of determination). Therefore, the trust we place in the values of the slopes, indicating the exponent of A in the Hopfinger and Toly's laws, should be limited and a simple power law between the turbulence intensity and the stroke amplitude may be inaccurate for the fractal I-shaped grid. This could be explained by the transport of the turbulence by the mean flow whose intensity and topology change with the stroke amplitude; for the small stroke amplitude ($A = 0.02$ m), the mean flow is directed towards the grid equilibrium position while it is globally directed towards the tank bottom and the water free surface for larger stroke amplitudes.

D. Study of the turbulence length scales

Based on the turbulent velocity fluctuations $\vec{v}'$, several length scales can be defined and linked to the large or small eddies generated in the flow whose associated kinetic energy follow the energy cascade highlighted by Kolmogorov[45]; the large turbulence structures transferring their kinetic energy to the smaller ones until viscous effects degrade it. Thus, the integral, the Taylor and the Kolmogorov length scales are going to be discussed in this result subsection.

1. Study of the integral length scales of turbulence

The integral length scales of turbulence, associated to the large turbulence structures (the large eddies), can be obtained from the auto-correlation curves of the turbulent velocity fluc-

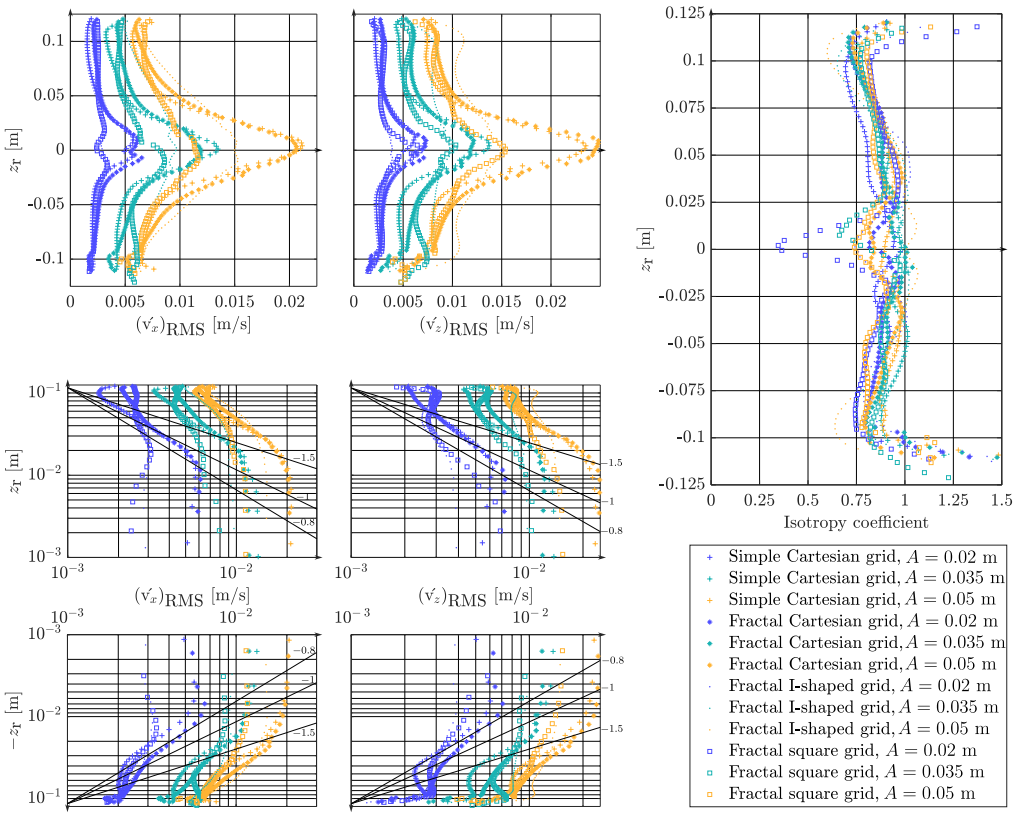

Figure 6. Vertical profiles of the RMS values of the turbulent fluctuations $(v'_x)_{RMS}$ and $(v'_z)_{RMS}$ in linear and logarithmic scales and vertical profiles of the isotropy coefficient (the ratio between $(v'_x)_{RMS}$ and $(v'_z)_{RMS}$) for the four grids and the three stroke amplitudes with $\nu = 1$ Hz at the central vertical plane.

Table IV. Features of the linear regressions between $(v'_i)_{RMS}\ z_r\, A^{-1.5}\, L_{mesh}^{-0.5}$ and ν used to check the exponent of ν in the Hopfinger and Toly's laws.

		$A = 0.02$ m		$A = 0.035$ m		$A = 0.05$ m	
		Slope	R^2	Slope	R^2	Slope	R^2
Horizontal component	Simple Cartesian grid	0.245	0.9978	0.233	0.9961	0.229	0.9989
	Fractal Cartesian grid	0.421	0.9979	0.384	0.9992	0.347	0.9981
	Fractal square grid	0.437	0.9973	0.391	0.9914	0.335	0.9997
	Fractal I-shaped grid	0.362	0.9956	0.971	0.9871	1.364	0.9998
Vertical component	Simple Cartesian grid	0.292	0.9957	0.260	0.9961	0.251	0.9995
	Fractal Cartesian grid	0.494	0.9993	0.446	0.9998	0.397	0.9970
	Fractal square grid	0.495	0.9965	0.453	0.9990	0.387	0.9984
	Fractal I-shaped grid	0.388	0.9856	1.163	0.9949	1.647	0.9993

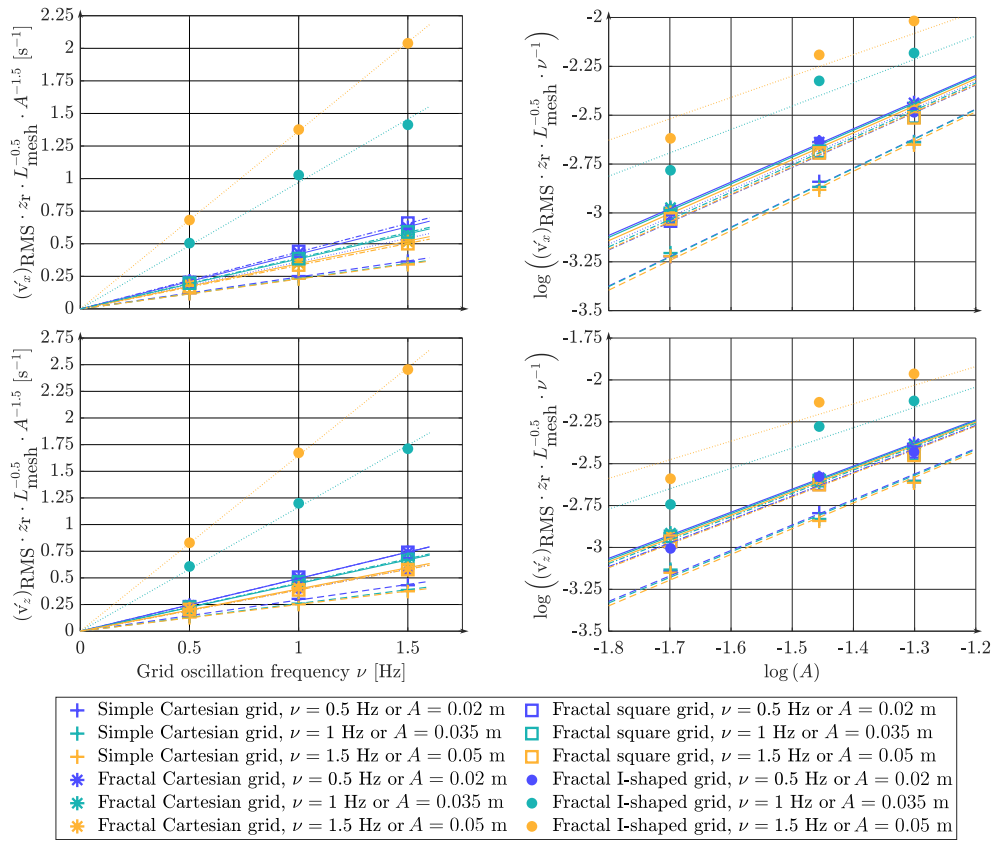

Figure 7. Linear regressions checking the ν and A exponents in the Hopfinger and Toly's laws for the four grids used at the central vertical plane (the dashed lines are relative to the simple Cartesian grid, the solid lines to the fractal Cartesian grid, the dash-dotted lines to the fractal square grid and the dotted lines to the fractal I-shaped grid).

Table V. Features of the linear regressions between $\log\left((v_i)_{\mathrm{RMS}}\ z_{\mathrm{r}}\ \nu^{-1}\ L_{\mathrm{mesh}}^{-0.5}\right)$ and $\log(A)$ used to check the exponent of A in the Hopfinger and Toly's laws.

		$\nu = 0.5$ Hz		$\nu = 1$ Hz		$\nu = 1.5$ Hz	
		Slope	R^2	Slope	R^2	Slope	R^2
Horizontal component	Simple Cartesian grid	1.509	0.9956	1.511	0.9957	1.521	0.9956
	Fractal Cartesian grid	1.365	0.9994	1.371	0.9971	1.380	0.9985
	Fractal square grid	1.406	0.9949	1.398	0.9887	1.405	0.9921
	Fractal I-shaped grid	1.390	0.9799	1.197	0.9233	1.095	0.9062
Vertical component	Simple Cartesian grid	1.521	0.9846	1.526	0.9738	1.535	0.9776
	Fractal Cartesian grid	1.378	0.9995	1.383	0.9950	1.389	0.9948
	Fractal square grid	1.405	0.9974	1.395	0.9793	1.409	0.9897
	Fractal I-shaped grid	1.405	0.9767	1.215	0.9219	1.113	0.8906

tuations as eddies can be seen as space regions where velocities are correlated. In our case with a two-dimensional and two components PIV method, four auto-correlation functions can be defined: $R_{\acute{v}_x,x}$ and $R_{\acute{v}_x,z}$, respectively the auto-correlation of the horizontal component of the turbulent velocity fluctuations along a horizontal and a vertical direction, and $R_{\acute{v}_z,x}$ and $R_{\acute{v}_z,z}$, their equivalent for the vertical component of the turbulent velocity fluctuations. Thus for each spatial point (x,z), the four auto-correlation curves, function of the shift steps Δx or Δz (see equations 16 and 17), can be drawn (in our case, the curves with positive and negative shift steps were averaged into a single curve per point) and integral length scales $L_{I,\acute{v}_x,x}$, $L_{I,\acute{v}_x,z}$, $L_{I,\acute{v}_z,x}$ and $L_{I,\acute{v}_z,z}$ can be obtained by computing the surface under the associated auto-correlation curve (see equation 18, the integrals were evaluated thanks to the trapeze method). Finally, the global horizontal and the global vertical integral length scales can be computed (see equation 19) by assuming a horizontally isotropic turbulence[23] because we have only access to $\acute{v}_x$ and $\acute{v}_z$, not to $\acute{v}_y$.

$$R_{\acute{v}_i,x}(x,z,\Delta x) = \frac{\overline{\acute{v}_i(x,z,t)\,\acute{v}_i(x+\Delta x,z,t)}}{\sqrt{\overline{(\acute{v}_i(x,z,t))^2}\;\overline{(\acute{v}_i(x+\Delta x,z,t))^2}}} \tag{16}$$

$$R_{\acute{v}_i,z}(x,z,\Delta z) = \frac{\overline{\acute{v}_i(x,z,t)\,\acute{v}_i(x,z+\Delta z,t)}}{\sqrt{\overline{(\acute{v}_i(x,z,t))^2}\;\overline{(\acute{v}_i(x,z+\Delta z,t))^2}}} \tag{17}$$

$$L_{I,\acute{v}_i,j}(x,z) = \int_0^\infty R_{\acute{v}_i,j}(x,z,\Delta j)\,d\Delta j \tag{18}$$

$$L_{I,i} = \sqrt{2\,{L_{I,\acute{v}_x,i}}^2 + {L_{I,\acute{v}_z,i}}^2} \tag{19}$$

The values of the global integral length scales for each spatial point (x,z) can be summarised by averaging them line by line to obtain the vertical profiles $L_{I,i}(z)$. These vertical profiles of integral length scales are depicted in the left-hand part of the figure 8 for the four grids with each oscillation frequency and each stroke amplitude.

In a general way, the oscillation frequency has no significant impact on the integral length scales whatever the grid while the impact of the stroke amplitude seems to depend on the considered grid geometry. Indeed, for the simple Cartesian grid, the curves are more clearly separated according to the stroke amplitude than for the other grid geometries; the greater the stroke amplitude, the less the integral length scales increase away from the grid wake region for the simple Cartesian grid. For the three other fractal grids, the nine curves more or less overlap and no dependence with A seems significant or direct. This specific feature of the simple Cartesian grid compared to the fractal grids can be explained by the fractal nature of these last ones. Indeed, as the fractal grid possess several bar widths thanks to the different fractal iterations, eddies with a larger range of length scales can be present directly in the vicinity of the grid wake region leading to a standardisation of the curves. In addition, it appears quite difficult to link the order of magnitude of the integral length scales with the geometric parameters as the stroke amplitudes, the grid mesh sizes or the grid bar widths since whatever the grid geometry, the stroke amplitude or the oscillation frequency, the integral length scale values globally lie between 0.01 and 0.025 m.

About the impact of the boundary conditions, the horizontal and the vertical integral length scales drop as reaching the tank bottom or the water free surface due to the vortex compression near the surfaces[21]. For the Cartesian grids, the decreases start between 0.045 and 0.05 m from the tank bottom or the water free surface. For the fractal square and I-shaped grids, the decrease of the vertical integral length scales starts more or less 0.05 m away from the grid equilibrium position while the horizontal integral length scales drastically drop 0.01 m from the tank bottom or the water free surface.

Like the inversely proportional relation between the RMS values of the turbulent velocity fluctuations and the coordinate z_r, Hopfinger and Toly confirmed a linear relation between the integral length scale and z_r initially proposed by Thompson and Turner. For the Cartesian grids, this linear relation seems confirmed in the region not affected by boundary conditions but with a higher proportionality coefficient - between 0.2 and 0.25 instead of 0.1 as initially proposed - especially for the small stroke amplitude (0.02 m) and beneath the grid equilibrium position. For the fractal square and I-shaped grids, such a linear relation can be confirmed in a tiny region between 0.02 and 0.025 m around the grid equilibrium position with a proportionality coefficient of 0.25.

As indicated in the first section of this article, a turbulence-based Reynolds number Re_I can be defined with the RMS values of the turbulent velocity fluctuations and the integral length scales (see equation 6). Thus, the vertical profiles of this turbulent Reynolds number Re_I for the four grids and for each oscillation frequency and each stroke amplitude are depicted in the right-hand part of the figure 8. According to the definition of this Reynolds number and the Hopfinger and Toly's laws for the vertical profiles $(\acute{v}_i)_{\mathrm{RMS}}$ and $L_{I,i}$, the vertical profiles of Re_I should be independent of z_r. This is the case for the simple Cartesian grid with $A = 0.02$ and 0.035 m and especially for fractal Cartesian grid in a certain range of z_r: from about 0.02 or 0.025 m away from z_{eq} to about 0.020 or 0.03 m from the tank bottom or the free surface. For the fractal square and I-shaped grids with large stroke amplitudes, linear relations seem to appear between Re_I and z_r in a comparable range of z_r. As the z_r exponent in the Hopfinger and Toly's laws and the linear relations between the integral length scales and z_r were not verified, especially for the fractal square and I-shaped grids, such an independence with z_r was not expected.

2. *Study of the Taylor length scales of turbulence*

The Taylor length scales of turbulence can be obtained from the auto-correlation curves of the turbulent velocity fluctuations, matching with the zero of the parabola tangent to the auto-correlation curve at the intercept. Therefore, it depends on the decrease of the auto-correlation curve and is associ-

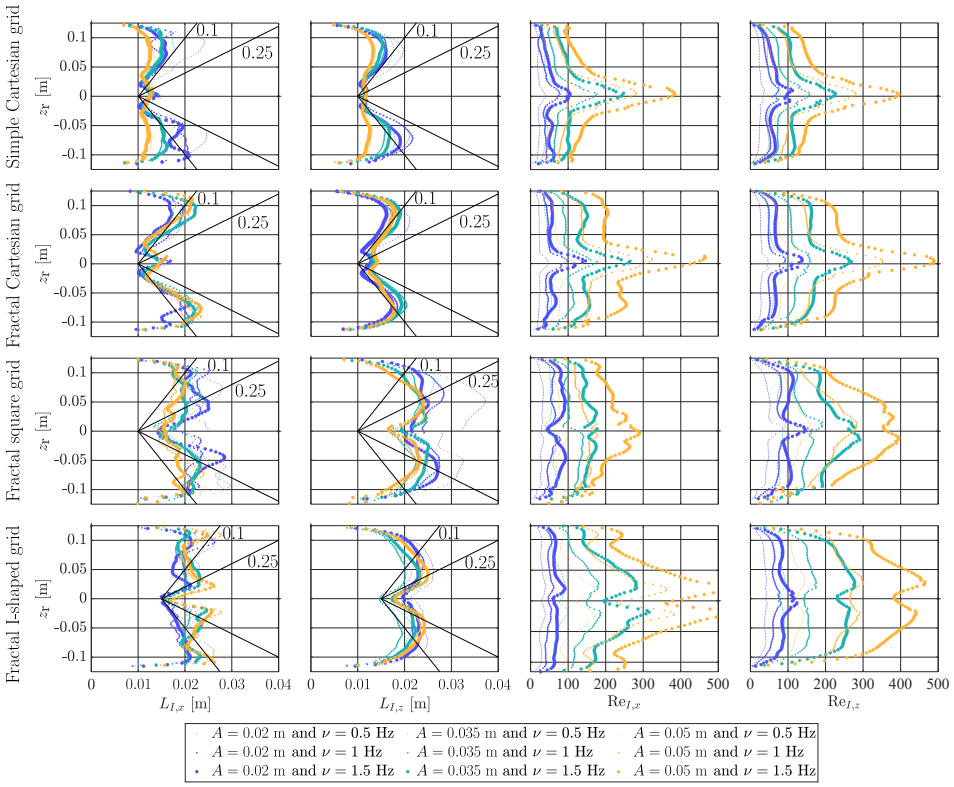

Figure 8. Vertical profiles of the integral length scales and the associated Reynolds numbers for the four grids at the central vertical plane.

ated to the gradient of the turbulent velocity fluctuations. As for the integral length scales, four Taylor length scales $L_{T,\nu'_x,x}$, $L_{T,\nu'_x,z}$, $L_{T,\nu'_z,x}$ and $L_{T,\nu'_z,z}$ can be defined. Thanks to the equation similar to the equation 19, the global horizontal and vertical Taylor length scales can be computed. The left-hand part of the figure 9 depicts the vertical profiles of the Taylor length scales for the four grids at the central vertical plane computed in a similar way than the vertical profiles of the integral length scales (by averaging the data line by line). As for the integral length scales, one may define a turbulence-based Reynolds number Re_T by using the Taylor length scales instead of the integral length scales with the RMS values of the velocity turbulent fluctuations. Thus, the vertical profiles of the turbulent Reynolds number associated to the Taylor length scales are depicted in the right-hand part of the figure 9 for the four grids and for each oscillation frequency and each stroke amplitude.

As for the integral length scale, there is no significant dependence between the Taylor length scales and the grid oscillation frequency and the stroke amplitude except for the simple Cartesian grid for which the curves are separated according to the stroke amplitude: the larger the stroke amplitude, the lower the Taylor length scales. As the computation of the Taylor length scales is based on the auto-correlation curves like the integral length scales, this phenomenon can be explained by the multiscale nature of the fractal grids too. Globally, the Taylor length scales lie between 0.01 and 0.015 m and overlap with the integral length scales in the grid wake region. Conversely to the integral length scales which rise away from the grid and drop near tank bottom and the free surface, the Taylor length scales tend to remain constant and drop near the boundaries of the fluid domain, except for the fractal Cartesian grid whose Taylor and integral length scales follow similar trends. Based on this last remark, the vertical profiles of the Taylor length scales-based turbulent Reynolds number Re_T are similar to the vertical profiles of the RMS values of the turbulent velocity fluctuations. Power laws between Re_T and z_r (with the z_r exponent equal to 1) seem accurate for the Cartesian grids while linear dependencies seem more accurate for the fractal square grid and especially for the fractal I-shaped grid for large stroke amplitudes. This last behaviour

could be linked to the interactions between the turbulence and the mean flow. Indeed, as the presence of significant mean flows is known to disturb the turbulence propagation away from the grid[65], the specific mean flows generated by the fractal square and the fractal I-shaped grids mainly depending on the grid pattern itself (conversely to the Cartesian grids) could disturb the turbulence propagation in the tank and leading to this linear behaviour (conversely to the power laws more accurate for the Cartesian grids.

3. Study of the Kolmogorov length scales

The last turbulence length scale, associated to the smallest turbulence structures dissipated by viscous effects, is the Kolmogorov length scale L_K. This last one can be estimated thanks to the mean turbulent dissipation rate $\overline{\varepsilon}$ and by considering isotropic and homogeneous turbulence (see equations 20 and 21) as only two velocity components are provided by the classical PIV method[12,45]. The spatial derivatives of the turbulent velocity fluctuations were computed by a central difference scheme of the finite difference method (scheme decreasing the discretisation error compared to first order schemes like the forward or the backward difference schemes). As a reminder, the PIV image resolution is 750 by 750 pixels resulting in a vector field resolution of 90 by 90 vectors. Therefore, the vector field resolution is, in terms of real length, about 0.0028 m which is not sufficient to properly capture the smallest turbulence structures. It should thus be reminded at this point that what is presented below only deals with estimations of the Kolmogorov length scales (based on assumptions).

$$\overline{\varepsilon} = \frac{3\,\mu}{\rho}\left(\overline{\left(\frac{\partial \acute{v}_x}{\partial x}\right)^2} + \overline{\left(\frac{\partial \acute{v}_z}{\partial z}\right)^2} + \overline{\left(\frac{\partial \acute{v}_x}{\partial z}\right)^2} + \overline{\left(\frac{\partial \acute{v}_z}{\partial x}\right)^2} + 2\,\overline{\left(\frac{\partial \acute{v}_x}{\partial z}\,\frac{\partial \acute{v}_z}{\partial x}\right)} + \frac{2}{3}\,\overline{\left(\frac{\partial \acute{v}_x}{\partial x}\,\frac{\partial \acute{v}_z}{\partial z}\right)}\right) \tag{20}$$

$$L_K = \sqrt[4]{\frac{\mu^3}{\rho^3\,\overline{\varepsilon}}} \tag{21}$$

From the equations 20 and 21, a value for the Kolmogorov length scale can be assigned to each spatial point (x,z) and the figure 10 displays the vertical profiles of the Kolmogorov length scales for each grid, each oscillation frequency and each stroke amplitude obtained by averaging the data line per line.

Conversely to the integral and the Taylor length scales, the curves of the Kolmogorov length scales do not overlap each other and the more intense the turbulence (i.e. the higher the global RMS values of the turbulent velocity fluctuations), the lower the global Kolmogorov length scale. In addition, the more intense the turbulence, the flatter the curves indicating that the Kolmogorov length scales seem to be limited to minimum values. To illustrate this, the figure 11 displays the minimum value of the vertical profiles of the Kolmogorov length scale for each grid function of an oscillation-based Reynolds number[23,35] $\mathrm{Re}_{\mathrm{osc}}$ incorporating the oscillation frequency ν and the stroke amplitude A. Power laws were applied on the data points indicating that high oscillation frequencies and large stroke amplitudes are required to reach low Kolmogorov length scales. The difference between the curves related to the Cartesian grids and the ones related to the two other fractal grids seem to lie in the way the laser plane cuts the grid bars: in the lengthwise direction for the Cartesian grids and laterally for the fractal square and I-shaped grids.

$$\mathrm{Re}_{\mathrm{osc}} = \frac{\rho\,\nu\,A^2}{\mu} \tag{22}$$

E. Study of the turbulence spectra

Spatial and time spectra of turbulence can be used to summarise information on the turbulence length scales and to assess the isotropic and homogeneous nature of turbulence. Four spatial spectra of turbulence, function of the wave number (inverse of a length, a kind of spatial frequency), are obtained by taking the discrete Fourier transform of the auto-correlation curves $\overline{\acute{v}_i(x,z,t)\,\acute{v}_i(x+\Delta x,z,t)}$ and $\overline{\acute{v}_i(x,z,t)\,\acute{v}_i(x,z+\Delta z,t)}$, while two time spectra of turbulence, function of the time frequency (inverse of a time), can be obtained by taking the discrete Fourier transform of the time auto-correlation curves $\overline{\acute{v}_i(x,z,t)\,\acute{v}_i(x,z,t+\Delta t)}$. To highlight the frequency content of the oscillatory flow, spatial and time spectra can be obtained from the auto-correlation curves of the sum of the oscillatory flow and the turbulent velocity fluctuations $\bar{v}_i(x,z,t)+\acute{v}_i(x,z,t)$. The spectra resolution and length depend on the auto-correlation increments Δx, Δz and Δt (the smaller the increments, the finer the spectra resolution), on the fluid domain size (L_{tank}) for the spatial spectra and on the time series length for the time spectra. In practice, the spatial and time spectra were obtained by applying the Fast Fourier Transform (FFT) algorithm of Matlab on each auto-correlation curve associated to each spatial point (x,y). We should mention a specificity for the time spectra: as the moving masks used to hide the grid and the grid support bars during the PIV treatment induce missing data in the time series of the masked points, no time spectrum can be computed for these points contained in the grid wake region.

The figure 12 presents the different global spatial spectra of the auto-correlation curves for the four grids and for each stroke amplitude with the grid oscillation frequency $\nu = 1$ Hz (only the spectra with this grid oscillation fre-

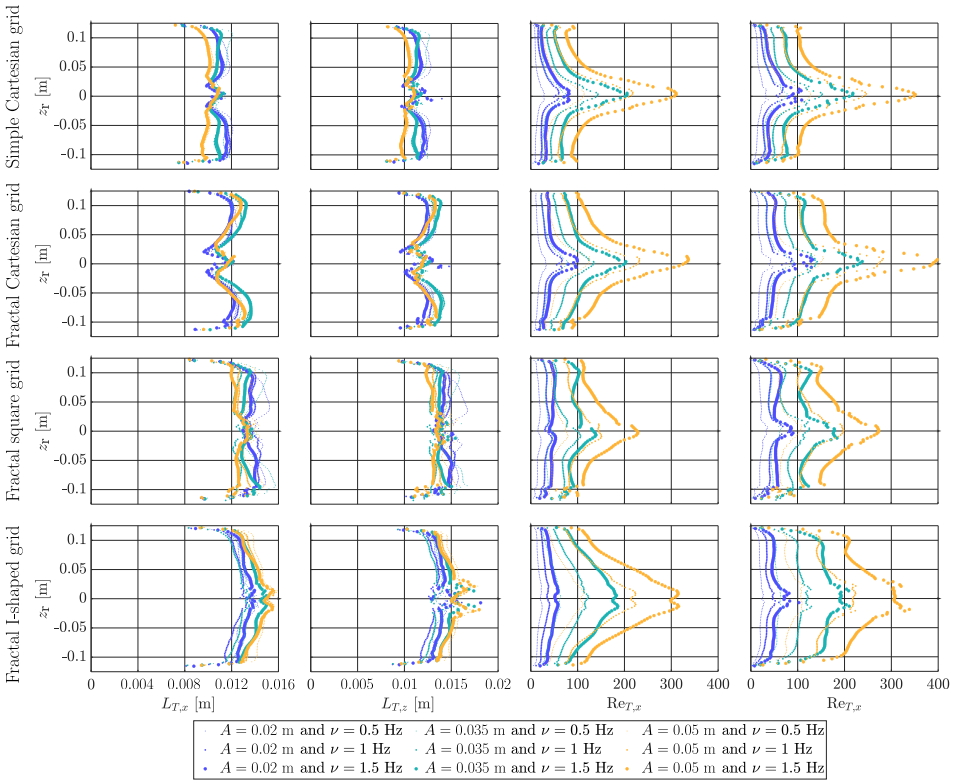

Figure 9. Vertical profiles of the Taylor length scales and the associated Reynolds numbers for the four grids at the central vertical plane.

quency were displayed for legibility concerns and as the spectra shapes seem not affected by ν). Each global spectrum was obtain by averaging all the spectra over the space domain (x,y). Only the spectra related to the auto-correlations of the horizontal (respectively vertical) velocity components along the x (respectively z) axis were considered and displayed. The straight inclined black line on each graph indicates the classical $-5/3$ slope of isotropic turbulence[45]; the turbulence spectra for the fractal grids are more closely aligned with this line between the wave numbers 10 and 100 m^{-1}, especially for the fractal square and I-shaped grids. The spectra related to the auto-correlation of the sum of the turbulent fluctuations and the oscillatory flow can be used to highlight the size of characteristic flow structures. Thus, the grid mesh size L_{mesh} (indicated by vertical red lines on the left graphs of the figure 12) of the simple Cartesian grid is emphasised on the spectra of the auto-correlations $\overline{(\acute{\mathrm{v}}_x(x,z,t)+\widetilde{\mathrm{v}}_x(x,z,t))\,(\acute{\mathrm{v}}_x(x+\Delta x,z,t)+\widetilde{\mathrm{v}}_x(x+\Delta x,z,t))}$ (the dashed curves on the left graphs of the figure 12) whatever the stroke amplitude while it is not the case for the other fractal grids (with lower grid mesh sizes due to their fractal nature). For these last ones except the fractal I-shaped grid, the corresponding spectra indicate small peaks for lower wave numbers apparently related to the quarter of the water tank side length $L_{\mathrm{tank}} = 0.249$ m or the distance between the largest central bar (fractal iteration 0) and the bar of the first fractal iteration for the fractal Cartesian grid. No distinctive horizontal flow structure length seems highlighted on the spectra of the fractal I-shaped grid. About the spectra of $\overline{(\acute{\mathrm{v}}_z(x,z,t)+\widetilde{\mathrm{v}}_z(x,z,t))\,(\acute{\mathrm{v}}_z(x,z+\Delta z,t)+\widetilde{\mathrm{v}}_z(x,z+\Delta z,t))}$ (the dashed curves on the right graphs of the figure 12), the highlighted vertical flow structure lengths seem linked to the stroke amplitude: the sizes of the flow structures created in the grid wake, smaller than the grid stroke amplitude, are highlight by small bumps in the the spectra especially for $A = 0.02$ m whatever the grid. This phenomenon seems mitigated for larger stroke amplitudes which can be explained by the easier disengagement of the eddies behind the grids. To conclude about these space spectra, we should temperate our interpretations due to the investigated range of wave numbers limited by

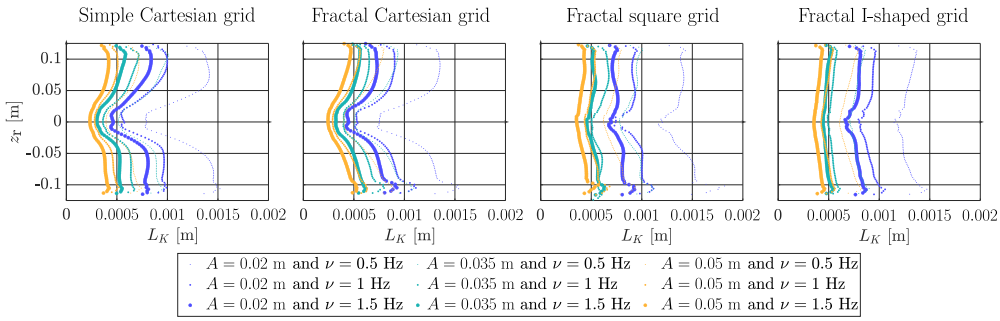

Figure 10. Vertical profiles of the Kolmogorov length scales for the four grids at the central vertical plane.

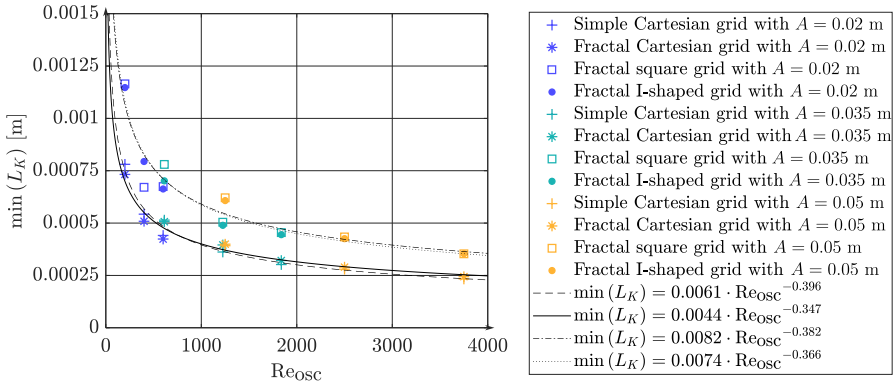

Figure 11. Minimum values of the Kolmogorov length scales for the four grids at the central vertical plane function of the oscillation-based Reynolds number (the dashed curve stands for the power law regression of the data related to the simple Cartesian grid, the solid curve to the fractal Cartesian grid, the dash-dotted curve to the fractal square grid and the dotted curve to the fractal I-shaped grid).

the space resolution of the original flow fields (the maximum wave numbers equal $1/(2\,\Delta x)$ or $1/(2\,\Delta z)$); thus the ranges of the Taylor and Kolmogorov length scales are not depicted.

The figure 13 displays the different time spectra of the auto-correlation curves for the four grids and for each stroke amplitude with the grid oscillation frequency $\nu = 1$ Hz (only the spectra with this grid oscillation frequency were displayed for legibility concerns and as the spectra shapes seem not affected by ν). As for the space spectra above, each global time spectrum was obtained by averaging all the available spectra over the space domain (x,y). As for the space spectra, the straight inclined black line on each graph indicates the classical $-5/3$ slope of isotropic turbulence. The alignments between this straight line and the time spectra are less marked than in the cases of the space spectra; the slopes of the time spectra are closer to -2 than to $-5/3$. The ranges of the integral time scale, defined in a similar way to the integral length scale as the surface below the time auto-correlation curves (see equation 23), are displayed beneath the time spectra of turbulence on the figure 13 while the ranges of the Kolmogorov time scales[45], estimated thanks to the mean turbulent dissipation rate $\overline{\varepsilon}$ (see equation 24), are depicted above the time spectra of turbulence. The fractal nature of the grids seems to increase the separation between the ranges of the integral time scales and the Kolmogorov time scales. The ranges of the integral time scales are globally centered around the grid oscillation frequency (the first peak in the time spectra related to the sum of the turbulent fluctuations and the oscillatory flow) while the higher harmonics of the oscillatory flow lie in the ranges of the Kolmogorov time scales.

$$t_{I,\hat{v}_i}(x,z) = \int_0^\infty R_{\hat{v}_i,t}(x,z,\Delta t)\,d\Delta t \tag{23}$$

$$t_K = \sqrt{\frac{\mu}{\rho\,\overline{\varepsilon}}} \tag{24}$$

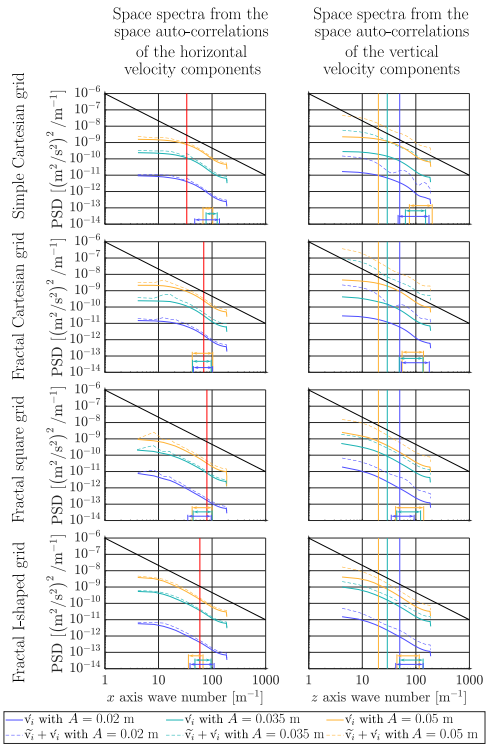

Figure 12. Global space spectra obtained from the auto-correlation curves of the turbulent velocity fluctuations and of the sum of these last ones and the oscillatory flow for each grid and the three stroke amplitudes with $\nu = 1$ Hz at the central vertical plane. The double arrow lines below the spectra indicate the range of frequencies related to the integral length scales; their colors are related to the associated stroke amplitude. The straight inclined black line on each graph has the classical $-5/3$ slope. The vertical red line on the graphs related to the horizontal velocity components (on the left) stands for the wave number of the mesh size L_{mesh} of the considered grid while the vertical lines on the graphs of the vertical velocity component (on the right) indicate the wave numbers of the associated (by the color) stroke amplitude.

V. CONCLUSION

In this work, we report the first experimental characterisation of turbulent flows generated by fractal oscillating grids. Time-resolved two-dimensional and two components PIV was used to probe the flow produced by four grids - a simple Cartesian grid (our reference case), a fractal Cartesian grid, a fractal square grid and a fractal I-shaped grid - oscillating with three stroke amplitudes A (0.02, 0.035 and 0.05 m) and three frequencies ν (0.5, 1 and 1.5 Hz) at the central vertical plane of a cubic water volume . Triple Reynolds decomposition was applied to characterise mean (time averaged), oscillatory (phase dependent) and turbulent velocity components. Several flow properties were studied to draw a general description of the flows generated by fractal oscillating grids with low oscillation frequencies: the intensity and the topology of the mean and the oscillatory flows, the root mean square (RMS) values of the turbulent velocity fluctuations, the turbulent length scales and the turbulence spatial and time spectra.

In the considered range of frequencies (from 0.5 to 1.5 Hz), the oscillation frequency globally acts linearly on the intensity of the mean flow, the oscillatory flow and the turbulent velocity fluctuations. It is shown by the velocity fields (normalised by the maximum grid velocity $\max\left(v_{\text{grid}}\right) = A\,\pi\,\nu$) of the flow statistics displaying no significant difference of intensity for the different oscillation frequencies by considering the same grid and the same stroke amplitude. Another clue in favour of this linear dependence between the grid oscillation frequency and the flow statistics intensity is the validation, for each grid, of the direct proportionality between the RMS values of the turbulent velocity fluctuations and the oscillation frequency highlighted in the Hopfinger and Toly's laws. Conversely to the oscillation frequency, an increase of the stroke amplitude impacts the flow topologies and intensities: for large strokes (0.035 and 0.05 m), the mean and oscillatory flow structures present with a small stroke (0.02 m) are emphasised (especially for the Cartesian grids and the fractal square grid) and the orientation of the mean flow can be inverted for the fractal I-shaped grid indicating a change in the flow regime with A (in relation with the KC number). The proportionality between the RMS values of the turbulent velocity fluctuations and $A^{1.5}$ indicated in the Hopfinger and Toly's laws is well verified for the simple Cartesian grid while different exponents seem more accurate for the fractal Cartesian and the fractal square grids (between 1.36 and 1.4). A power law with A seems inaccurate for the fractal I-shaped grid as the mean flow magnitude and global direction can affect the turbulence transport.

For each grid and whatever the oscillation frequency and the stroke amplitude, the mean flow is not negligible anywhere in the flow fields, as expected from the unfavorable conditions purposely chosen in that sense. The oscillatory flow is the most energetic contribution to the global flows but is essentially constrained in the grid wake region. The mean flow is generally oriented toward the tank bottom and the water free surface except for the fractal square grid for every A and ν and the fractal I-shaped grid at low stroke amplitude ($A = 0.02$ m) where the mean flow is globally directed toward the core region of the water volume. The oscillatory flow is mainly composed of counter-rotating vortices around and behind the grid bars.

The power laws indicated by the Hopfinger and Toly's laws for the vertical profiles of the RMS values of the turbulent velocity fluctuations were verified with an exponent for the vertical coordinates z_r (relative to the equilibrium position of the grid z_{eq}) lying between -0.8 and -1 for the simple Cartesian grid while these relations do not hold for the three other fractal grids. This can be explained by significant mean flows transporting turbulence away from the grid wake region, especially for the fractal I-shaped grid. In a general way, the

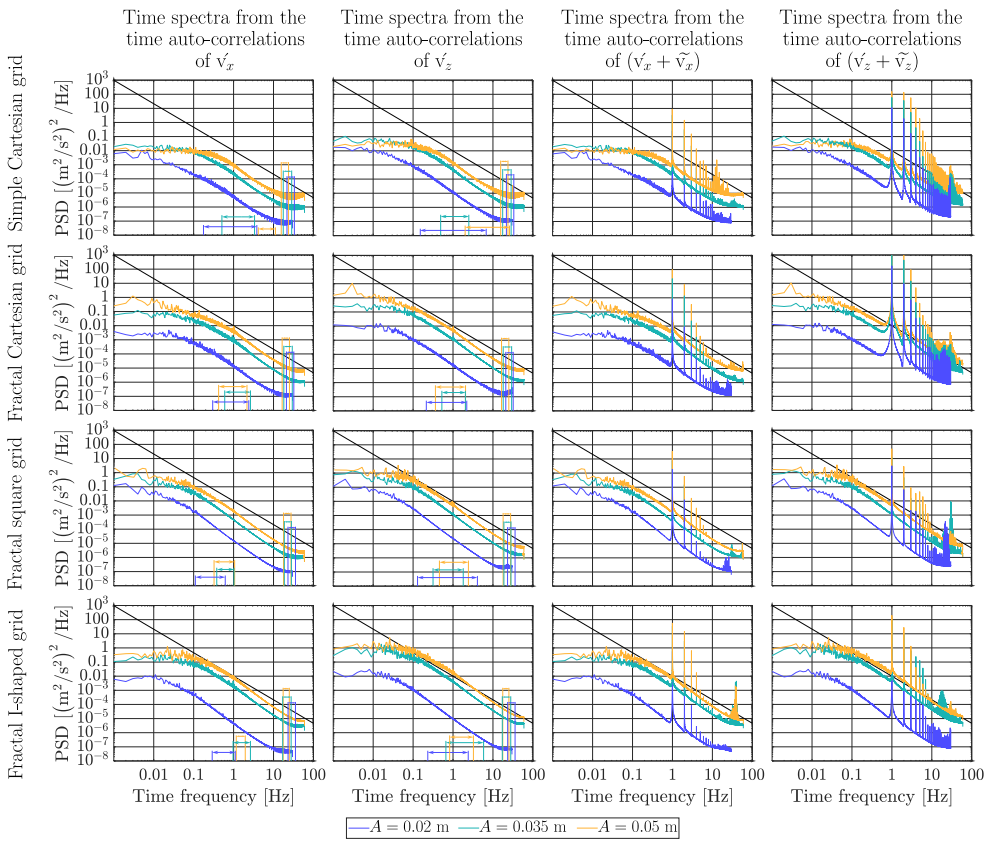

Figure 13. Global time spectra obtain from the auto-correlation curves of the turbulent velocity fluctuations and of the sum of these last ones and the oscillatory flow for each grid and the three stroke amplitudes with $\nu = 1$ Hz at the central vertical plane. The double arrow lines below the spectra indicate the ranges of frequencies related to the integral time scales while the double arrow lines above the spectra stand for the ranges of frequencies related to the Kolmogorov time scales; their colors are related to the associated stroke amplitude. The straight inclined black line on each graph has the classical $-5/3$ slope.

fractal character of the grids tends to increase the turbulence intensity and its propagation in the fluid medium except for the fractal square grid due to the mean flow converging in the core region.

Whatever the grid, the integral and Taylor length scales of turbulence respectively lie between 0.01 and 0.025 m and between 0.01 and 0.015 m with no clear link with the stoke amplitude or the oscillation frequency as all the vertical profiles tend to overlap each other. A notable exception is reported for the simple Cartesian grid, for which the larger the stroke amplitude, the smaller the integral and the Taylor length scales away from the grid wake region. Conversely, the higher the oscillation frequency or the larger the stroke amplitude, the lower the Kolmogorov length scales globally lying between 0.00025 and 0.0015 m. The fractal nature of the grids however tends to flatten the vertical profiles of the turbulence length scales, especially for the fractal square and I-shaped grids.

Although the flow field resolution limits the length of the turbulence space spectra, the global space spectra indicate a good agreement with the classical $-5/3$ slope of isotropic turbulence while the global time spectra indicate slopes closer to -2 whatever the grid geometry and the oscillation parameters ν and A.

With all that in mind, one may choose a grid and oscillation parameters to achieve a desired flow topology and magnitude (for the mean and the oscillatory flows and for the turbulent fluctuations) with manageable turbulence length scales (especially the Kolmogorov length scales): the frequency acts

linearly on the magnitude of the flows without significantly affecting the integral and Taylor length scales. In turn, the amplitude can affect the spatial distribution and propagation of the flows. The minimum Kolmogorov length scales are manageable by the oscillation-based Reynolds number (combining A and ν). The choice of the fractal pattern remains the most impacting about all these flow properties.

It is worth remembering that only the central vertical plane of each grid was analysed in every cases and analyses of other PIV planes should be considered to fully characterise the flows generated by fractal oscillating grids and their three-dimensional structure. To that effect, three-dimensionnal Particle Tracking Velocimetry (PTV) experiments and numerical simulations could complete this study of fractal oscillating grid flows. The ranges of the experimental parameters (the stroke amplitude, the oscillation frequency, the grid blockage ratio, the number of grids, ...) could be expanded in further works to assess the limits and the validity of our conclusions. This work still provides basis and a set of indications on conditions to manage the flow topologies, magnitudes and length scales and to achieve optimal turbulence intensity enhancement and spreading with fractal oscillating grids, suggesting promising potential applications to chemical and biochemical processes as mixing devices.

ACKNOWLEGEMENTS

This work was partially funded by the French National Research Agency (IFrOG project, ANR-22-CE51-0015-01) and by a doctoral scholarship granted by the University of Mons and Institut Mines Télécom Nord Europe.

DATA AVAILABILITY STATEMENT

The data that support the findings of this study are available from the corresponding author upon reasonable request.

Appendix: Flow statistics convergence study

This appendix is dedicated to the convergence study of the flow statistics mentioned in the fourth point "Flow statistics and Reynolds triple decomposition" of the third section "Equipment and flow visualisation method" of this article. This convergence study was performed by considering the number of grid oscillation periods for the central plane of the simple Cartesian grid with $A = 0.05$ m, $\nu = 0.5$ Hz. The figure 14 summarises the results of this convergence study by considering the flow statistics data obtained from a Reynolds triple decomposition: the mean flow and the RMS values of the oscillatory flow and the turbulent fluctuations. This convergence study indicates that 1000 grid oscillation periods are largely sufficient for all statistical quantities to converge.

REFERENCES

[1] Al-Homoud, A. and Hondzo, M., "Enhanced uptake of dissolved oxygen and glucose by Escherichia coli in a turbulent flow," Applied Microbiology and Biotechnology **79**, 643–655 (2008).
[2] An, H., Cheng, L., and Zhao, M., "Direct numerical simulation of oscillatory flow around a circular cylinder at low keulegan-carpenter number," Journal of Fluid Mechanics **666**, 77–103 (2011).
[3] Arnott, R. N., Cherif, M., Bryant, L. D., and Wain, D. J., "Artificially generated turbulence: a review of phycological nanocosm, microcosm, and mesocosm experiments," Hydrobiologia **848**, 961–991 (2021).
[4] Atkinson, J. F., Damiani, L., and Harleman, D. R. F., "A comparison of velocity measurements using a laser anemometer and a hot-film probe, with application to grid-stirring entrainment experiments," Physics of Fluids **30**, 3290 (1987).
[5] Brumley, B. H. and Jirka, G. H., "Near-surface turbulence in a grid-stirred tank," Journal of Fluid Mechanics **183**, 235–263 (1987).
[6] Carter, D., Petersen, A., Amili, O., and Coletti, F., "Generating and controlling homogeneous air turbulence using random jet arrays," Experiments in Fluids **57**, 189 (2016).
[7] Cheng, N.-S. and Law, A. W.-K., "Measurements of Turbulence Generated by Oscillating Grid," Journal of Hydraulic Engineering **127**, 201–208 (2001).
[8] Comte-Bellot, G. and Corrsin, S., "The use of a contraction to improve the isotropy of grid-generated turbulence," Journal of Fluid Mechanics **25**, 657–682 (1966).
[9] Connolly, J. P., Armstrong, N. E., and Miksad, R. W., "Adsorption of Hydrophobic Pollutants in Estuaries," Journal of Environmental Engineering **109**, 17–35 (1983).
[10] Crawley, G., Gruy, F., and Cournil, M., "In-line study of crystal fragmentation in a stirred reactor," Chemical Engineering Science **51**, 4537–4550 (1996).
[11] Dohan, K. and Sutherland, B., "Turbulence time scales in mixing box experiments," Experiments in Fluids **33**, 709–719 (2002).
[12] Doron, P., Bertuccioli, L., Katz, J., and Osborn, T. R., "Turbulence characteristics and dissipation estimates in the coastal ocean bottom boundary layer from PIV data," Journal of Physical Oceanography **31**, 2108–2134 (2001).
[13] Dütsch, H., Durst, F., Becker, S., and Lienhart, H., "Low-reynolds-number flow around an oscillating circular cylinder at low keulegan-carpenter numbers," Journal of Fluid Mechanics **360**, 249–271 (1998).
[14] Elias, C. B. and Joshi, J. B., "Role of hydrodynamic shear on activity and structure of proteins," in *Bioprocess and Algae Reactor Technology, Apoptosis*, Vol. 59 (Springer Berlin Heidelberg, 1998) pp. 47–71, series Title: Advances in Biochemical Engineering Biotechnology.
[15] Escudié, R. and Liné, A., "Experimental analysis of hydrodynamics in a radially agitated tank," AIChE Journal **49**, 585–603 (2003).
[16] Fernando, H. J. S. and De Silva, I. P. D., "Note on secondary flows in oscillating-grid, mixing-box experiments," Physics of Fluids A: Fluid Dynamics **5**, 1849–1851 (1993).
[17] Gogate, P. R., Beenackers, A. A., and Pandit, A. B., "Multiple-impeller systems with a special emphasis on bioreactors: a critical review," Biochemical Engineering Journal **6**, 109–144 (2000).
[18] Hannoun, I. A., Fernando, H. J. S., and List, E. J., "Turbulence structure near a sharp density interface," Journal of Fluid Mechanics **189**, 189–209 (1988).
[19] Hopfinger, E. J. and Toly, J.-A., "Spatially decaying turbulence and its relation to mixing across density interfaces," Journal of Fluid Mechanics **78**, 155–175 (1976).
[20] Huang, G., Lv, X., Chen, W., Song, Y., Yin, J., and Wang, D., "Generation of nearly homogeneous isotropic turbulence using a novel oscillating grid system," Physics of Fluids **36**, 035129 (2024).
[21] Hunt, J. C. R. and Graham, J. M. R., "Free-stream turbulence near plane boundaries," Journal of Fluid Mechanics **84**, 209 (1978).
[22] Hurst, D. and Vassilicos, J. C., "Scalings and decay of fractal-generated turbulence," Physics of Fluids **19**, 035103 (2007).
[23] Janzen, J. G., Herlina, H., Jirka, G. H., Schulz, H. E., and Gulliver, J. S., "Estimation of mass transfer velocity based on measured turbulence parameters," AIChE Journal **56**, 2005–2017 (2010).

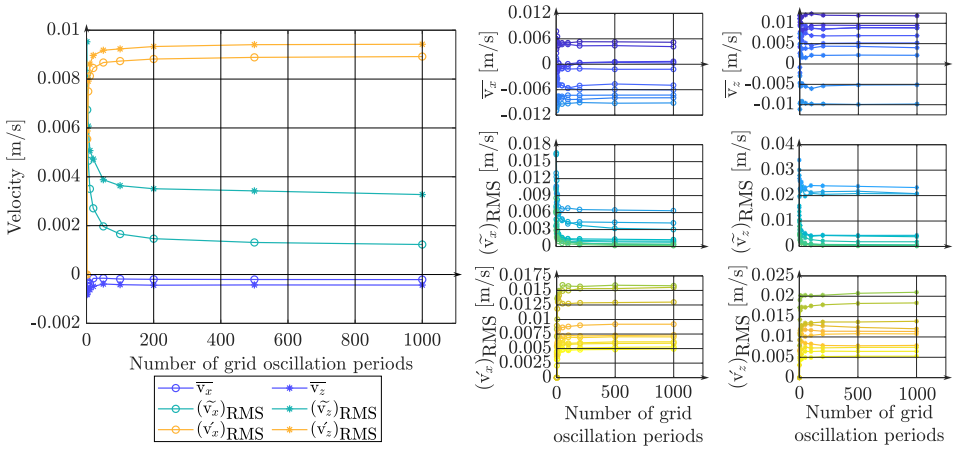

Figure 14. Preliminary convergence study for the flow statistics (mean flow and RMS values of the oscillatory flow and the turbulent fluctuations) for the central vertical plane of the simple Cartesian grid with $A = 0.05$ m and $\nu = 0.5$ Hz. The graph on the left displays the values of the statistical indicators spatially averaged over the whole x and z plane while each curve in the six graphs on the right stands for 10 random points in the x and z plane (for these six graphs, the curve color has no special meaning, it is used to distinguish between curves).

[24]Kang, H. S., Chester, S., and Meneveau, C., "Decaying turbulence in an active-grid-generated flow and comparisons with large-eddy simulation," Journal of Fluid Mechanics **480**, 129–160 (2003).
[25]Kistler, A. L. and Vrebalovich, T., "Grid turbulence at large reynolds numbers," Journal of Fluid Mechanics **26**, 37 (1966).
[26]Kitamura, T., Nagata, K., Sakai, Y., Sasoh, A., Terashima, O., Saito, H., and Harasaki, T., "On invariants in grid turbulence at moderate reynolds numbers," Journal of Fluid Mechanics **738**, 378–406 (2014).
[27]Kolmogorov, A. N., "Dissipation of energy in the locally isotropic turbulence," Proceedings: Mathematical and Physical Sciences **434**, 15–17 (1991).
[28]Kolmogorov, A. N., "The local structure of turbulence in incompressible viscous fluid for very large reynolds numbers," Proceedings of the Royal Society of London. Series A: Mathematical and Physical Sciences **434**, 9–13 (1991).
[29]Lacassagne, T., Lyon, A., Simoëns, S., Hajem, M. E., and Champagne, J.-Y., "Flow around an oscillating grid in water and shear-thinning polymer solution at low Reynolds number," Experiments in Fluids **61**, 15 (2020).
[30]Lacassagne, T., Simoëns, S., EL Hajem, M., Lyon, A., and Champagne, J.-Y., "Oscillating grid turbulence in shear-thinning polymer solutions," Physics of Fluids **31**, 083102 (2019).
[31]Laizet, S. and Vassilicos, J. C., "DNS of fractal-generated turbulence," Flow, Turbulence and Combustion **87**, 673–705 (2011).
[32]Li, Q. and Cheng, N.-S., "Experimental investigation of characteristics of turbulence induced by multiple oscillating grids," Physics of Fluids **36**, 035140 (2024).
[33]Luo, C., Guo, L., Zeng, S., and Long, T., "Effects of turbulence fluctuation intensity in bioreactor of sewage treatment on physical and chemical properties of biofilms," Bioprocess and Biosystems Engineering **44**, 1865–1874 (2021).
[34]Masaló, I., Guadayol, Ò., Peters, F., and Oca, J., "Analysis of sedimentation and resuspension processes of aquaculture biosolids using an oscillating grid," Aquacultural Engineering **38**, 135–144 (2008).
[35]Matsunaga, N., Sugihara, Y., Komatsu, T., and Masuda, A., "Quantitative properties of oscillating-grid turbulence in a homogeneous uid," Fluid Dynamics Research (1999).
[36]McCorquodale, M. W. and Munro, R., "Direct effects of boundary permeability on turbulent flows: observations from an experimental study using zero-mean-shear turbulence," Journal of Fluid Mechanics **915**, A134 (2021).
[37]McCorquodale, M. W. and Munro, R. J., "A method for reducing mean flow in oscillating-grid turbulence," Experiments in Fluids **59**, 182 (2018).
[38]Mcdougall, T. J., "Measurements of turbulence in a zero-mean-shear mixed layer," Journal of Fluid Mechanics **94**, 409–431 (1979).
[39]McKenna, S. P. and McGillis, W. R., "Observations of flow repeatability and secondary circulation in an oscillating grid-stirred tank," Physics of Fluids **16**, 3499–3502 (2004).
[40]Mordant, N., "Experimental high reynolds number turbulence with an active grid," American Journal of Physics **76**, 1092–1098 (2008).
[41]Nagami, Y. and Saito, T., "An Experimental Study of the Modulation of the Bubble Motion by Gas–Liquid-Phase Interaction in Oscillating-Grid Decaying Turbulence," Flow, Turbulence and Combustion **92**, 147–174 (2014).
[42]Nienow, A. W., "Reactor engineering in large scale animal cell culture," Cytotechnology **50**, 9–33 (2006).
[43]Nokes, R. I., "On the entrainment rate across a density interface," Journal of Fluid Mechanics **188**, 185–204 (1988).
[44]Orlins, J. J. and Gulliver, J. S., "Turbulence quantification and sediment resuspension in an oscillating grid chamber," Experiments in Fluids **34**, 662–677 (2003).
[45]Pope, S. B., *Turbulent flows*, cambridge university press ed. (Cornell University, New York, 2000).
[46]Raffel, M., Willert, C. E., Scarano, F., Kähler, C. J., Wereley, S. T., and Kompenhans, J., *Particle Image Velocimetry: A Practical Guide* (Springer International Publishing, Cham, 2018).
[47]Reynolds, W. C. and Hussain, A. K. M. F., "The mechanics of an organized wave in turbulent shear flow. Part 3. Theoretical models and comparisons with experiments," Journal of Fluid Mechanics **54**, 263–288 (1972).
[48]Rouse, H. and Dodu, J., "Diffusion Turbulente à Travers Une Discontinuité de Densité," La Houille Blanche **41**, 522–532 (1955).
[49]Roustan, M., Liné, A., and Pharamond, J.-C., "Agitation. mélange - concepts théoriques de base," Techniques de l'ingénieur Opérations unitaires. Génie de la réaction chimique (2023), 10.51257/a-v2-j3800.
[50]San, L., Long, T., and Liu, C., "Algal Bioproductivity in Turbulent Water: An Experimental Study," Water **9**, 304–312 (2017).
[51]Shy, S., Jang, R., and Tang, C., "Simulation of Turbulent Burning Velocities Using Aqueous Autocatalytic Reactions in a Near-Homogeneous Turbulence," Combustion and Flame **105**, 54–62 (1996).

[52]Shy, S., Tang, C., and Fann, S., "A nearly isotropic turbulence generated by a pair of vibrating grids," Experimental Thermal and Fluid Science **14**, 251–262 (1997).
[53]Silva, I. P. D. D. and Fernando, H. J. S., "Some aspects of mixing in a stratified turbulent patch," Journal of Fluid Mechanics **240**, 601 (1992).
[54]Tatsuno, M. and Bearman, P. W., "A visual study of the flow around an oscillating circular cylinder at low keulegan-carpenter numbers and low stokes numbers," Journal of Fluid Mechanics **211**, 157–182 (1990).
[55]Thielicke, W. and Sonntag, R., "Particle Image Velocimetry for MATLAB: Accuracy and enhanced algorithms in PIVlab," Journal of Open Research Software **9**, 12 (2021).
[56]Thompson, S. M. and Turner, J. S., "Mixing across an interface due to turbulence generated by an oscillating grid," Journal of Fluid Mechanics **67**, 349–368 (1975).
[57]Tikhomirov, V. M., "On the degeneration of isotropic turbulence in an incompressible viscous fluid," in *Selected Works of A. N. Kolmogorov*, edited by V. M. Tikhomirov (Springer Netherlands, 1991) pp. 319–323.
[58]Tsai, C.-H. and Lick, W., "A Portable Device for Measuring Sediment Resuspension," Journal of Great Lakes Research **12**, 314–321 (1986).
[59]Variano, E. A. and Cowen, E. A., "A random-jet-stirred turbulence tank," Journal of Fluid Mechanics **604**, 1–32 (2008).
[60]Veit, D., "Polyamide," in *Fibers* (Springer International Publishing, 2022) pp. 649–680.
[61]Villermaux, E., Sixou, B., and Gagne, Y., "Intense vortical structures in grid-generated turbulence," Physics of Fluids **7**, 2008–2013 (1995).
[62]Wang, C. and Lan, C. Q., "Effects of shear stress on microalgae - a review," Biotechnology Advances **36**, 986–1002 (2018).
[63]Watanabe, T., Sakai, Y., Nagata, K., Ito, Y., and Hayase, T., "Implicit large eddy simulation of a scalar mixing layer in fractal grid turbulence," Physica Scripta **91**, 074007 (2016).
[64]Weitemeyer, S., Reinke, N., Peinke, J., and Hölling, M., "Multi-scale generation of turbulence with fractal grids and an active grid," Fluid Dynamics Research **45**, 061407 (2013).
[65]Yan, J., Cheng, N.-S., Tang, H.-W., and Tan, S. K., "Oscillating-grid turbulence and its applications: a review/ Turbulence de grille oscillante et ses applications: une revue," Journal of Hydraulic Research **45**, 26–32 (2007).
[66]Yao, H., Cao, L., Wu, D., Gao, Y., Qin, S., and Yu, F., "PIV study on grid-generated turbulence in a free surface flow," Water **13**, 909 (2021).
[67]Yao, N., Wang, Y., Liu, J., Sun, X., Hao, Z., Liu, Y., Chen, S., and Wang, G., "Bubble rise characteristics in oscillating grid turbulence," Minerals Engineering **164**, 106832 (2021).
[68]Yi, Y.-K. and Lyn, D. A., "Scaling and Inhomogeneities in Oscillating-Grid Flows," Water Resources , 10 (2004).
[69]Yousuf, M. and Frawley, P. J., "Secondary nucleation from nuclei breeding and its quantitative link with fluid shear stress in mixing: A potential approach for precise scale-up in industrial crystallization," Organic Process Research & Development **23**, 926–934 (2019).